Time course of alterations in adult spinal motoneuron properties in the SOD1(G93A) mouse model of ALS

Seoan Huh[1], Charles J. Heckman[1,2,3], and Marin Manuel[1,4,§]

[1]Department of Physiology, [2]Department of Physical Medicine and Rehabilitation, and [3]Department of Physical Therapy and Human Movement Science, Northwestern University, Feinberg School of Medicine, Chicago, Illinois, USA. [4]Université de Paris, SPPIN - Saints-Pères Paris Institute for the Neurosciences, CNRS, Paris, France.

§ Corresponding author:

Marin MANUEL
SPPIN - Saints-Pères Paris Institute for the Neurosciences
Université de Paris, 45, rue des Saints-Pères, 75006 Paris, France
email: marin.manuel@neurobio.org

Author contribution

Conceptualization: S.H., C.J.H., and M.M.; Methodology: S.H., C.J.H., and M.M.; Investigation: S.H.; Formal analysis: S.H. and M.M.; Software: M.M.; Visualization: S.H. and M.M.; Writing - Original Draft: S.H.; Writing - Review & Editing: S.H., C.J.H., and M.M.; Funding Acquisition: C.J.H and M.M.; S.H., C.J.H., and M.M. approved the final version of this manuscript.

Conflict of Interest

The authors have no conflict of interest to declare

Acknowledgments

This work was supported by NIH NINDS R01NS077863 and NINDS R01NS110953. S.H. was supported by a National Science Foundation Graduate Research Fellowship (NSF GRFP).

Abstract

Although ALS is an adult-onset neurodegenerative disease, motoneuron electrical properties are already altered during embryonic development. Motoneurons must therefore exhibit a remarkable capacity for homeostatic regulation to maintain a normal motor output for most of the life of the patient. In the present paper, we demonstrate how maintaining homeostasis could come at a very high cost. We studied the excitability of spinal motoneurons from young adult SOD1(G93A) mice to end-stage. Initially homeostasis is highly successful in maintaining their overall excitability. This initial success, however, is achieved by pushing some cells far above the normal range of passive and active conductances. As the disease progresses, both passive and active conductances shrink below normal values in the surviving cells. This shrinkage may thus promote survival, implying the previously large values contribute to degeneration. These results support the hypothesis that motoneuronal homeostasis may be "hyper-vigilant" in ALS and a source of accumulating stress.

Significance Statement

During ALS, motoneurons exhibit a remarkable ability to maintain a normal motor output despite continuous alterations of their electrophysiological properties, up to the point when overt symptoms become apparent. We show that this homeostatic process can sometimes push motoneurons beyond the normal range, which may be causing long-lasting harm.

Introduction

ALS is a fatal neurodegenerative disorder characterized by progressive loss of cortical and spinal motoneurons. Five to ten percent of the ALS cases are familial (FALS), and ~20% of the FALS cases are due to mutations in the Superoxide Dismutase1 (SOD1) gene (Rosen et al., 1993). Studies in the mutant SOD1 (mSOD1) mouse and other animal models have revealed that multiple cellular functions become impaired as the disease progresses (Ilieva et al., 2009; Kanning et al., 2009; Johnson and Heckman, 2010; Brownstone and Lancelin, 2018), implying that homeostatic mechanisms are failing. Yet, despite an early surge in motoneuron excitability in the embryonic state (Kuo et al., 2004; van Zundert et al., 2008; Pieri et al., 2009; Martin et al., 2013), mutant mice maintain a normal motor output for several months, suggesting the involvement of very potent and effective homeostatic process to maintain the intrinsic excitability of the motoneurons.

The standard measure of the net excitability of motoneurons is the relation between the frequency of firing and the amplitude of the injected current. Multiple ionic currents contribute to this frequency-current (F-I) function relationship. Chief among them are persistent inward currents (PICs), which are mediated by voltage-gated Na+ and Ca2+ channels. In neonatal mSOD1 mice, PICs in spinal motoneurons become aberrantly large (Quinlan et al., 2011). On its own, this change would increase F-I gain, but it is compensated by commensurate increases in the leak currents that set the input conductance of the cell, so that the net excitability remains constant (Quinlan et al., 2011). These abnormal changes show that F-I homeostasis during the neonatal period is achieved via a compensatory mechanism.

72 If, however, these compensatory increases persist into the young adult state, then
73 the continued distortions in input conductances and PIC amplitudes could induce a
74 substantial stress within the motoneurons. Increasing the number of leak
75 conductances and voltage-gated channels implies a higher energy expenditure to
76 maintain the resting membrane potential and ionic gradients across the membrane,
77 which already occupies a large share of the metabolic budget of neurons (Attwell
78 and Laughlin, 2001; Herculano-Houzel, 2011; Howarth et al., 2012). One must also
79 consider the additional burden associated with the increased housekeeping tasks
80 such as lipid synthesis, trafficking of organelles and protein synthesis, which
81 account for 25–50% of the energy budget of neurons (Rolfe and Brown, 1997;
82 Attwell and Laughlin, 2001). In this scenario, the initial success in the homeostatic
83 regulation of net excitability would come at a severe cost, likely accelerating the
84 onset of degeneration. Indeed, neurons function on a very restricted energy budget
85 that is independent of their size (Herculano-Houzel, 2011). On the other hand, if
86 homeostatic processes instead successfully return input conductance and PIC values
87 to normal ranges before the onset of denervation, then homeostasis for the F-I
88 function would reduce stress on the cell and effects on subsequent degeneration
89 would likely be small.

90 Here, we investigated how the homeostatic processes required to maintain
91 normal excitability (current onset and F-I gain) develop as the disease progresses.
92 We undertook the first *in vivo* voltage-clamp studies of motoneurons in the
93 SOD1(G93A) mouse model of ALS and pursued these measurements across a wide
94 range of ages, from P30 to P120. This age range spans the young adult period, the

95 onset of denervation period (~P50, Pun et al., 2006), and the development of overt
96 symptoms (~P90). Because adult mSOD1 motoneurons tend to have a larger input
97 conductance than controls (Delestrée et al., 2014), we hypothesized that input
98 conductance and PIC values would continue to grow in the young adult state. Our
99 results supported this hypothesis, revealing, in fact, a continual increase in the
100 amplitude of these parameters, followed by a collapse, so that motoneurons
101 surviving beyond the onset of overt symptoms (~P90) had aberrantly small values
102 of each. These results are consistent with the possibility that homeostasis for
103 excitability is not weak but excessively strong and that this overreaction contributes
104 to subsequent degeneration (Mitchell and Lee, 2012).

105 # Methods

106 ## Animals

107 This study was performed in strict accordance with the recommendations in the
108 Guide for the Care and Use of Laboratory Animals of the National Institutes of
109 Health. All of the animals were handled according to protocols approved by
110 Northwestern University's institutional animal care and use committee (IACUC). All
111 surgery was performed under sodium pentobarbital anesthesia, and every effort
112 was made to minimize suffering. Because of the reproducible and stereotyped
113 progression of symptoms, we chose to use mice overexpressing the human
114 SOD1(G93A) gene, in which glycine has been substituted by alanine at residue 93 as
115 a mouse model of ALS. Hemizygous B6SJL.SOD1(G93A) transgenic mutant males
116 were bread with B6SJL F1 females (obtained from the Jackson Laboratory, Bar

117 Harbor, ME)(Leitner et al., 2009). Offspring were genotyped and the transgene copy
118 number was compared to a housekeeping gene at Transnetyx (Cordova, TN). Only
119 mice with relative copy number >45 were used in this study. The control group
120 consisted of non-transgenic littermates, with the same B6SJL background (WT). 33
121 animals of either sex were used in this study. Because these experiments tend to
122 have a higher success rate with larger animals, our sample was biased towards
123 males (27 males and 6 females). Animals were divided into different age groups for
124 analysis: animals whose age was <60 days-old were categorized as P30–60 (N=9
125 mice), animals whose age was ≥60 and <90 as P60–90 (N=12 mice), and animals
126 older than ≥90 days-old were classified as P90–120 (N=12 mice).

127 **In vivo preparation**

128 Procedures were similar to those in our previous studies (Manuel and Heckman,
129 2011). Initially, atropine (0.2 mg/kg) was administered subcutaneously to prevent
130 salivation. Ten minutes later, anesthesia was initiated with an intraperitoneal
131 injection of pentobarbital sodium (70 mg/kg) and maintained by intravenous
132 infusion of supplemental doses of pentobarbital (6 mg/kg) mixed in perfusion
133 solution containing 4% glucose, 1% $NaHCO_3$, and 14% Plasmion. The trachea was
134 cannulated, allowing the mouse to be artificially ventilated with 100% O_2. The end-
135 tidal PCO_2 was continuously monitored and maintained around 4% by adjusting
136 ventilator parameters including respiratory rate around 120–150 bpm and tidal
137 volume around 0.09–0.23 mL. The hind limb muscles were then dissected; biceps
138 femoris was removed to expose the sciatic nerve, which was thereafter placed over
139 a stimulating electrode. A laminectomy was performed at the T13–L1 level and the

140 L3–L4 spinal segments were exposed. To prevent the spinal cord from dehydration,
141 a custom made bath was affixed using silicone elastomer and covered with mineral
142 oil. To locate the motoneurons of interest, the sciatic nerve was stimulated at 1.8–2×
143 the minimum intensity required to observe an afferent volley.

144 **Electrophysiology**

145 Intracellular recordings of spinal motoneurons were performed by impaling them
146 with glass micropipette electrodes filled with 3M KCl with a resistance of 8–15 MΩ.
147 Motoneurons were identified by the presence of antidromic action potential from
148 stimulation of the sciatic nerve. Cells with unstable resting membrane potential
149 (RMP) or with RMP more depolarized than −50 mV were excluded from the analysis.
150 We record a median of 3 cells per animal (average ± SD 3.1±1.7 cells per animal,
151 mode 2 cells/animal, N=33).

152 PICs were recorded in discontinuous voltage-clamp mode, with switching rates of
153 6–8 kHz. Clamp feedback gain was between 0.3 and 1.5. In addition to the feedback
154 gain from the Axoclamp amplifier, an additional low-frequency feedback loop with a
155 gain of 11 and a cutoff of −3 dB at 0.3 kHz was used to improve voltage control in
156 such large cells as motoneurons (Lee and Heckman, 1998). Monitoring outputs were
157 observed at all times to assure reasonable settling of the electrode. To record PICs, a
158 slow triangular voltage ramp (−80 to −40 mV) was applied (Lee and Heckman,
159 1998). Leak current was determined by fitting a regression line through the
160 subthreshold region (−80 to −65 mV) of the I-V function. Then, this leak was
161 subtracted from the total function to determine the PIC amplitude (measured both
162 on the ascending and descending part of the ramp). In addition, the voltage at which

163 the PIC was maximal on each part of the ramp was recorded (PIC peak voltage). The
164 PIC onset voltage was estimated on the leak-subtracted trace as the point where the
165 curve started to visibly deviate downward from the horizontal. Input conductance
166 was estimated as the slope of the leak current.

167 To assess the intrinsic properties of the motoneuron in current-clamp mode, we
168 measured the frequency-current (F-I) relationship of action potential firing. The F-I
169 relationship was determined based on the firing produced by a triangular current
170 injection. The interspike frequency was then plotted against the intensity of the
171 injected current. All these measurements were carried out in the discontinuous
172 current-clamp mode of the Axoclamp 2A amplifier, with switching rates of 6–8 kHz.
173 Mouse motoneurons possess two regimes of firing: a sub-primary range of firing,
174 followed by a linear primary range (Manuel et al., 2009; Manuel and Heckman,
175 2011). The primary range was identified visually starting from the top of the ramp
176 and going backward towards the beginning (for the ascending ramp) of forward
177 towards the end (for the descending ramp). A linear portion of the instantaneous
178 frequency, with low variability, can generally be easily identified before a sudden
179 change of slope or an increase in firing variability. The "gain" of the F-I relationship
180 was determined by fitting a regression line over the linear range so identified
181 (separately on the ascending and descending phase of the ramp). The other
182 parameters measured in the F-I relationship were: the current at which the first
183 action potential (AP) fires on the ascending ramp (recruitment current). the current
184 at which the last AP fires on the descending ramp (current at de-recruitment); the
185 voltage threshold for spiking, which was determined as the voltage where the slope

186 of the membrane voltage reaches 10 mV/ms before the first AP (Sekerli et al., 2004);
187 the current and firing frequency at the transition between the sub-primary and
188 primary ranges (Manuel and Heckman, 2011).

189 ## Data analysis

190 Recordings were acquired and analyzed using Spike2 v.7 (CED, Cambridge, UK).
191 Data were analyzed using the scientific python (v.3.7.4) ecosystem: Pandas v.1.0.5
192 (McKinney, 2011), SciPy v.1.5.2 (Virtanen et al., 2020), DABEST v.0.3.0 (Ho et al.,
193 2019), statsmodels v.0.12.0 (Seabold and Perktold, 2010) and scikit-learn v.0.23.0
194 (Pedregosa et al., 2011). Figures were generated using matplotlib v.3.1.3 (Hunter,
195 2007) and seaborn v.0.10.0 (Waskom et al., 2020).

196 ## Statistical analysis

197 All data are reported as mean ± standard deviation with their respective sample
198 size. Each cell is treated as an independent observation, and the reported N refers to
199 the number of cells, unless otherwise specified. No test was performed to detect
200 outliers, and no data points were excluded from the analysis. When comparing
201 between WT and mSOD1 samples, we focus on estimation statistics that rely on
202 effect sizes and confidence intervals (95%CI), rather than null hypothesis
203 significance testing, as recommended by several scientific societies and editorial
204 boards (Bernard, 2019; Makin and Orban de Xivry, 2019; Wasserstein et al., 2019;
205 Michel et al., 2020). Unless otherwise specified, effect sizes are reported as
206 differences of means and Hedges' g (Hedges, 2016). Where appropriate, data are
207 presented as Cumming plots (Cumming, 2012) generated using DABEST. In these
208 plots, the raw data are plotted as swarms of points. In addition, the mean ± standard

209 deviation of each group is plotted as a notched line immediately to the right of each
210 group. The effect size and bootstrapped 95% CIs are plotted on separate axes
211 beneath the raw data. Confidence intervals were bias-corrected and accelerated, and
212 are displayed with the bootstrap distribution of the mean; resampling was
213 performed 5000 times (Ho et al., 2019). Welch's *t*-test (Welch, 1947) results are
214 provided for information only. ANCOVA was performed using statsmodels' OLS
215 routines, fitting the model "PIC amplitude ~ input conductance * Genotype". No
216 significant interaction term was detected for any of the age groups considered, and
217 the model was run again without interaction. Dimensionality reduction was
218 performed using scikit-learn's PCA. The 21 electrophysiological features (which did
219 not include genotype or age) of our dataset were centered and scaled then projected
220 on a 5D space. For analysis, only the first three principal components were
221 considered.

222 Results

223 We set out to compare neuronal excitability, in 103 motoneurons from
224 SOD1(G93A) mice (mSOD1; 53 motoneurons), and their non-transgenic (WT; 50
225 motoneurons) littermate, aged between 31 and 123 days old. Neuronal excitability
226 was estimated on the response of the motoneurons to a triangular ramp of current
227 in current-clamp mode. In addition, PICs were measured in each motoneuron using
228 a triangular voltage ramp in voltage-clamp mode. Most of the values measured on
229 the ascending and descending phases of the ramps, both in voltage-clamp and
230 current-clamp were very strongly correlated (PIC amplitude on ascending and

231 descending ramps: r^2=0.75; PIC onset voltage: r^2=0.89; PIC peak voltage: r^2=0.90;
232 recruitment and de-recruitment currents: r^2=0.90). For this reason, we will mostly
233 focus on the parameters measured on the ascending ramp.

234 Given the large period considered here, one also needs to consider whether
235 alterations in motoneuron properties were direct effects of the mutation or merely
236 shifts in the distribution of the properties caused by the progressive loss of a
237 fraction of the motoneurons, starting with the least excitable FF motoneurons (Pun
238 et al., 2006; Hegedus et al., 2007, 2008; Martínez-Silva et al., 2018). For this reason,
239 we have split our dataset into three age groups. First, the young adult group (P30–
240 60) corresponds to pre-symptomatic animals, with little to no neuromuscular-
241 junction denervation (denervation starts at >P50 in FF motor units (Pun et al.,
242 2006)). The presymptomatic group (P60–90) corresponds to a group where there
243 are no overt motor symptoms despite a substantial loss of distal axons (Pun et al.,
244 2006) and the beginning of cell death in the spinal cord (Kanning et al., 2009;
245 Lalancette-Hebert et al., 2016). The symptomatic group (P90–120) contains animals
246 showing overt motor symptoms, and which have lost a significant proportion of
247 their motoneurons, particularly in the FF and FR population. Because motoneurons
248 are still intact in the young adult group, changes in electrical properties can be
249 directly interpreted as the direct result of the mutation, rather than the result of a
250 shift in the population average caused by the loss of a fraction of the motoneurons.
251 This age group will therefore be the main focus of the rest of our analysis.

252 ### Motoneurons from young adult mutant mice have overly large PICs

253 In motoneurons, one of the major determinants of excitability are PICs, which
254 were measured in response to a slow (5 mV/s) ramp in voltage-clamp mode. The
255 amplitude of the PIC was measured on the leak-subtracted trace at the point where
256 the downward deflection of the trace was maximal (see Figure 1A–B). We also
257 measured the PIC activation voltage, and the voltage at which the PICs reached their
258 peak.

259 In WT animals, PIC amplitude remained roughly steady during the age period
260 studied (Figure 1C). However, in mSOD1 motoneurons, PIC amplitudes started
261 higher than in WT animals at the youngest stages, then decreased strikingly over
262 time (Figure 1C). When broken down by age groups (Figure 1D), our results show
263 that, in the young adult stage (P30–60), the SOD1 mutation lead to an almost 3×
264 increase in PIC amplitudes compared to WT motoneurons. This increase appears to
265 be a continuation of the trend observed in neonates, where PICs were already
266 increased ~2 fold compared to controls (Quinlan et al., 2011). In the
267 presymptomatic group (P60–90), however, mSOD1 PICs shrunk to the same
268 amplitude as WT motoneurons. At symptomatic stages (P90–120), the trend seen in
269 young animals is reversed: PICs are much smaller in mSOD1 motoneurons
270 compared to WT motoneurons (Table 1).

271 In addition to its effect on PIC amplitude, SOD1 mutation also affected the voltage
272 at which PICs are recruited. The "PIC onset voltage", measured as the voltage at the
273 point where the leak-subtracted motoneuron I-V curve initially begins to curve
274 downward, was hyperpolarized by 10 mV in young mSOD1 mice compared to WT

275 controls (WT: −58.03±6.35 mV, N=19 vs. mSOD1: −69.41±5.71 mV, N=15; g=−1.83
276 95%CI[−2.64−−0.78]; t(32)=5.49, p=5.1e−06), and then slowly increased over time
277 to match the value in WT motoneurons by endstage (Figure 1E). The SOD1 mutation
278 had a similarly large effect on the voltage at which the PIC reached its maximum in
279 young animals (WT: −43.83±4.79 mV, N=19 vs. SOD1: −52.32±4.20 mV, N=15;
280 g=−1.83 95%CI[−2.63−−1.04]; t(32)=5.50, p=4.8e−06). The peak voltage then
281 increased progressively over time, paralleling the onset voltage (Figure 1F).

282 These profound changes in PIC amplitude and activation voltage would be
283 expected to have an impact on the firing properties of motoneurons. We, therefore,
284 performed current-clamp recordings in the same motoneurons as above. Starting
285 from its natural resting membrane potential, we injected a triangular ramp of
286 current to elicit the repetitive firing of the motoneuron (Figure 2A–B), and
287 measured the voltage threshold for spiking on the first spike triggered by the ramp.
288 In concordance with the hyperpolarization of the PICs, spiking threshold was also
289 hyperpolarized in young animals (WT: −45.35±5.48 mV, N=19 vs. mSOD1:
290 −54.86±5.15 mV, N=14; g=−1.74 95%CI[−2.53−−0.81]; t(31)=5.10, p=1.9e−05), and
291 increased over time (Figure 1G).

292 **Young adult motoneurons are nonetheless not hyperexcitable**

293 Despite the large alterations in PIC amplitude and activation voltage and the
294 change in the voltage threshold for spiking, the excitability of the motoneurons was
295 remarkably unaffected by the SOD1 mutation, regardless of age. Excitability was
296 quantified using the intensity of the current required to elicit the first spike on the
297 ascending ramp ("recruitment current"). Although the recruitment current

298 decreased over time in mSOD1 animals (Figure 2C), this effect was mostly driven by
299 older animals (Figure 2D). Young adult (P30–60) mutant motoneurons, whose
300 neuromuscular junctions are just starting to be denervated, and pre-symptomatic
301 motoneurons (P60–90), which experience substantial denervation, did not require,
302 on average, less current to reach firing threshold than WT controls (Figure 2D). At
303 symptomatic stages (P90–120), the SOD1 mutation does lead to a decrease in the
304 recruitment current compared to WT animals (Figure 2D), which is probably caused
305 by the degeneration of the high threshold motoneurons at this stage.

306 Neuronal excitability depends not only on how much current is needed to start
307 firing, but also at what frequency the neuron is firing once it is recruited. We
308 quantified the firing frequency of the motoneurons by measuring the slope of the
309 frequency-current relationship. As shown previously (Manuel et al., 2009), most F-I
310 curves, regardless of age and genotype, showed a distinct sub-primary range (SPR)
311 with a steep slope and high variability followed by a linear phase called primary
312 range (PR). We used the "gain" of the motoneuron, i.e. the slope of the F-I curve in
313 the PR, as another measure of excitability of motoneurons. Despite the alterations in
314 PICs in mutant motoneurons, the gain of the motoneuron F-I curves was unaffected
315 by both age and mutation (Figure 2E–F).

316 **Compensatory changes responsible to maintain excitability**

317 The fact that young adult motoneurons are not hyperexcitable despite substantial
318 alterations in the PICs suggests that other compensatory mechanisms are acting to
319 preserve the functional output of the cells. Motoneuron input conductance is an
320 important factor controlling neuron excitability. We estimated the input

321 conductance of mSOD1 and WT motoneurons from the slopes of their I-V
322 relationships around the level of the resting membrane potential (see Figure 1 and
323 Methods). Input conductances of mSOD1 and WT motoneurons are plotted against
324 the age of the animal in Figure 3A. Consistent with the continuous increase in the
325 size of the animals over the age span studied, WT motoneurons exhibit a moderate
326 increase in input conductance in WT motoneurons over time (Figure 3A). On the
327 other hand, mSOD1 motoneurons showed the opposite trend (Figure 3A). Young
328 adult mutant motoneurons had an input conductance almost twice as high as WT
329 controls at P30–P60 (Figure 3B). This increase is relatively greater (~1.7 fold) than
330 that observed in neonatal motoneurons (~1.25 fold) (Quinlan et al., 2011),
331 suggesting that the trend for increased conductance has become stronger as the
332 animal matures into the young adult state. However, by the late pre-symptomatic
333 stage (P60–90), the mutation had no longer any effect on input conductance. Finally,
334 symptomatic (P90–120) mSOD1 motoneurons had a smaller input conductance than
335 WT controls (Figure 3B), but this difference could be due to the degeneration of the
336 largest, high-threshold units at this stage.

337 The increase in input conductance is not the only compensatory change
338 happening in young adult mutant motoneurons. In particular, one would have
339 expected the leftward shift in the activation voltage of PICs seen in these
340 motoneurons to have a profound impact on their firing behavior. This discrepancy
341 can be explained by a parallel hyperpolarization (by almost 10 mV) of the resting
342 membrane potential in young adult mSOD1 motoneurons (Figure 4, P30–60). This
343 effect is still observable at pre-symptomatic stages, but to a lesser degree (Figure 4,

344 P60–90). At symptomatic ages, however, mutant motoneurons had similar resting
345 membrane potentials as WT controls (Figure 4, P90–120).

346 When taking into account this hyperpolarization of the resting membrane
347 potential, the relative values of the voltage threshold for spiking (ΔV_{th}, difference
348 between the voltage threshold and the resting membrane potential), as well as the
349 relative activation voltage of the PICs (ΔV_{PIC}) and the relative voltage at the peak of
350 the PIC (ΔV_{peak}) were all similar between WT and mSOD1 motoneuron regardless of
351 age (Table 1), which suggest that these are the quantities that are homeostatically
352 regulated.

353 **Arms race between PICs and input conductance**

354 Our results show that, during the disease progression, motoneurons are actively
355 engaged in a homeostatic process to maintain their firing output. The ratio of PIC to
356 conductance is a major determinant of net excitability. If these two parameters grow
357 in proportion, then net excitability is likely to stay about the same (Huh et al., 2017).
358 We thus analyzed the relationship between PIC amplitude and input conductance
359 (Figure 5). In the young adult animals (Figure 5A), the majority of the mutant
360 motoneurons are clustered in the upper right-hand corner, with values of both
361 conductances and PIC amplitudes that are outside of the range of WT controls. Yet,
362 the slopes were similar for both groups (ANCOVA, no significant interaction
363 between input conductance and genotype on PIC amplitude, $t(30)=-0.590$, $p=0.560$),
364 and the mutation had only a negligible effect on the relationship between PIC
365 amplitude and conductance (ANCOVA, effect of mutation −0.40 95%CI[−6.73–5.92],
366 $t(30)=-0.130$, $p=0.898$). Therefore the relationship between PIC amplitude and

367 input conductance was the same in WT and mSOD1 mice. This implies that, in these
368 animals, the cells that are abnormally large (large input conductance) also have PICs
369 that have increased in proportion. It is plausible that this process would, by itself,
370 cause undue stress to the cell (Attwell and Laughlin, 2001; Herculano-Houzel, 2011;
371 Howarth et al., 2012), due to the high metabolic demand imposed by their large size,
372 as well as the potential massive influx of calcium caused by their abnormally large
373 PICs. At the pre-symptomatic stages, the WT and mSOD1 populations roughly
374 overlap (Figure 5B). At the symptomatic ages, the situation is reversed, with the
375 appearance of a cluster (N=6) of very small cells with very small PICs (Figure 5C).
376 These results show that the overall initial increase in PIC and conductance
377 amplitudes were driven by the SOD1 mutation generates a sub-population of
378 motoneurons with conductance and PIC amplitudes that are well above the normal,
379 WT range (P30–60). Then, as the disease progresses, the steady reduction in these
380 amplitudes is so strong that by P90–120, some of the surviving cells fall well below
381 the normal range.

382 **Some cells are hypoexcitable and cannot fire repetitively**

383 Despite the remarkable ability of spinal motoneurons to maintain their
384 excitability and firing output demonstrated above, some mSOD1 motoneuron
385 tended to lose their ability to fire repetitively as the disease progressed (Delestrée
386 et al., 2014; Martínez-Silva et al., 2018). Out of the 53 mutant motoneurons
387 recorded, 6 motoneurons could not fire repetitively to current ramps despite still
388 being able to fire a single or a few action potentials to current steps. Figure 6 shows
389 an example of such a motoneuron. Although those cells were not, on average, larger

390 than those that fired repetitively (Figure 6D), non-firing cells were characterized by
391 a very small PIC amplitude (Figure 6E, see also (Huh et al., 2017)). Finally, although
392 non-firing motoneurons could be recorded in WT mice (7 out of 50 motoneurons),
393 non-firing motoneurons appeared, on average, 25 days earlier in mSOD1 mice
394 (Figure 6F).

395 **Other motoneuron properties**

396 Given the large number of electrophysiological parameters measured in each cell
397 (21 per cell), we used Principal Component Analysis (PCA) to analyze the overall
398 behavior of the cells across time and genotype. The first three principal components
399 (PCs) accounted for 67% of the variance in the data (PC1: 33.8%, PC2: 21.4%, PC3:
400 11.9%). Figure $7A_{1-3}$ shows how the first three principal components varied with
401 the age of the animal in mSOD1 and WT mice. For WT mice, all principal
402 components were constant over time (slopes: PC1 0.102 AU/week 95%CI[−0.178–
403 0.381], r^2=0.024, p=0.459; PC2 −0.112 AU/week 95%CI[−0.368–0.144], r^2=0.034,
404 p=0.376; PC3 0.043 AU/week 95%CI[−0.182–0.269], r^2=0.007, p=0.694). On the
405 other hand, in mSOD1 mice, the first two principal components evolved over time.
406 PC1 started at a higher value than WT mice, decreased over time (slope
407 −0.460 AU/week 95%CI[−0.625–−0.295], r^2=0.450, p=1.6e−06), and became smaller
408 than in WT mice at endstage. PC2 followed the opposite trend. In young mSOD1
409 animals, PC2 was lower than in WT animals, and then it increased over time (albeit
410 by a very small amount; 0.151 AU/week 95%CI[0.006–0.296], r^2=0.102, p=0.042).
411 Finally, PC3 stayed constant (−0.089 AU/week 95%CI[−0.192–0.013], r^2=0.074,

412 p=0.086) and indistinguishable from WT. Higher principal components did not show
413 any dependency on age or genotype (not shown).

414 The opposite behavior of PC1 and PC2 in mSOD1 mice indicates that several
415 features are anti-correlated. PC1 was strongly positively correlated to input
416 conductance, as well as most current measurements (PIC amplitude, recruitment
417 current, etc.) (Figure 7B), which were also the features that were increased the most
418 in young adult mSOD1 vs. WT animals (Figure 7C, top rows). On the other hand, PC2
419 was more strongly correlated to voltage measurements (voltage threshold, PIC peak
420 voltage, PIC onset voltage, resting membrane potential; Figure 7B), which were
421 features that were strongly decreased in young adult mSOD1 vs. WT (Figure 7C,
422 bottom rows). Overall, PCA clearly highlights two sets of features that evolve in
423 opposite direction over time, presumably to compensate for one another in order to
424 maintain neuronal excitability as close to normal as possible.

425 Discussion

426 In this paper, we studied how motoneuron electrical properties evolve over the
427 time course of ALS, focusing particularly on the persistent inward currents (PICs).
428 We show that, in young adult mutant mice, before and up to the time when motor
429 unit denervation is just starting, PICs are abnormally large compared to controls.
430 This increase in PIC amplitude is accompanied by a parallel increase in motoneuron
431 input conductance with the net effect that the excitability of the cells remains
432 normal. Later, while the animals remain pre-symptomatic but denervation has
433 begun, motoneuron properties return to normal levels. Finally, in symptomatic

434 animals, mutant motoneurons tend to have smaller input conductance and smaller
435 recruitment current, which is most likely due to the death of the largest, low
436 threshold cells at this stage.

437 ## Homeostatic regulation of motoneuron output

438 Although ALS is classically considered an adult-onset disease, we know from
439 earlier studies of motoneurons in animal models of ALS that the change in
440 motoneurons' intrinsic excitability is the first sign to be seen in the pathogenesis,
441 long before any overt motor deficits manifest. Hyperexcitability is observed in
442 cultured E13 spinal motoneurons (Kuo et al., 2004), E15 cortical motoneurons (Pieri
443 et al., 2009), E17.5 spinal motoneurons (Martin et al., 2013 p.20), as well as early
444 postnatal hypoglossal motoneurons (van Zundert et al., 2008). Consequently, the
445 motor system in general, and motoneurons in particular, must exhibit remarkable
446 capability for homeostatic regulation to maintain a quasi-normal motor output until
447 overt symptoms appear, but there are many combinations of intrinsic properties
448 that can produce the same firing pattern (Marder and Goaillard, 2006). In neonatal
449 mSOD1 mice, the majority of motoneurons exhibited normal excitability (based on
450 recruitment current and F-I gain), although the most resistant population of
451 motoneuron seem to retain some hyperexcitability (Quinlan et al., 2011; Leroy et al.,
452 2014). Yet, PICs were almost twice as large in mutant compared to WT neonatal
453 motoneurons (Quinlan et al., 2011). This increased PIC amplitude was seemingly
454 compensated by a parallel increase in input conductance (Quinlan et al., 2011). In
455 adults, this trend seems to continue, particularly in the young adult age group.
456 Global analysis of our dataset using PCA shows that, generally speaking, currents

457 tend to be much bigger in young adult mSOD1 mice compared to WT (we observe an
458 almost 3× increase in PIC amplitude, accompanied by an almost 2× increase in input
459 conductance), which then tend to decrease over time. This increase is accompanied
460 by a hyperpolarization of the PIC onset and peak voltages, but which are
461 compensated by a commensurate hyperpolarization of the resting membrane
462 potential. These trends with disease progression from the embryonic state through
463 the development of severe symptoms are summarized in Figure 8. An overall
464 pattern of oscillations is evident, with the PIC oscillations tending to increase
465 excitability but the conductance and rest potential oscillations tending to reduce it.

466 The properties of the motoneurons seem to normalize at the late pre-
467 symptomatic stage (P60–90), but it is unclear whether this is due to changes in the
468 homeostatic pathways involved, or whether it is caused by the start of the
469 degeneration process in the most vulnerable motoneurons. At symptomatic stages,
470 motoneurons appear to be hyper-excitable. They have, on average, a smaller input
471 conductance (Figure 3), and smaller recruitment current (Figure 2), but that most
472 likely reflect the fact that the largest cells have degenerated by this age, and that the
473 remaining cells may have shrunk (see below, and Dukkipati et al., 2018). In addition,
474 it should be noted that a small but growing number of cells become incapable of
475 firing repetitively at this stage (Delestrée et al., 2014; Martínez-Silva et al., 2018).

476 **The hidden cost of excitability homeostasis**

477 Although the degeneration of motoneurons in ALS constitutes a failure in cell
478 homeostasis, our results show that, throughout the "silent", presymptomatic phase

479 of ALS, motoneurons are actively engaged in a highly successful homeostatic process
480 to maintain their firing output, and thereby producing a normal motor behavior.

481 The driving force behind this homeostatic process remains mysterious. Although
482 it is commonly agreed that intracellular calcium plays a major role in this process
483 (Turrigiano et al., 1994; O'Leary et al., 2010; O'Leary and Wyllie, 2011), this calcium
484 can enter the cell through various channels (e.g. synaptic receptors, voltage-
485 dependent calcium channels) and the location and pattern of that calcium signal
486 could potentially have distinct downstream targets. We demonstrated here that
487 motoneurons can maintain a normal firing output through most of the pre-
488 symptomatic phase of the disease in response to current injected through the
489 microelectrode. Yet, during behavior, motoneurons are activated through synaptic
490 inputs, most of which are impinging on the dendritic tree. Bączyk, Ouali Alami et al.
491 (2020) have recently demonstrated that excitatory synaptic inputs are depressed in
492 pre-symptomatic mSOD1 mice. Excitability homeostasis, therefore, cannot be
493 restricted to the intrinsic properties of motoneurons, but potentially involve the
494 whole sensorimotor network. Indeed, in the motor cortex, although several cell
495 types (including corticospinal pyramidal cells) were found to be intrinsically
496 hyperexcitable in symptomatic mSOD1 mice, the activity of corticospinal pyramidal
497 neurons during behavior (measured by two-photon calcium imaging during head-
498 fixed locomotion) was indistinguishable from controls (Kim et al., 2017). Whether
499 network-level homeostasis and intrinsic excitability homeostasis are parallel,
500 independent, processes, or whether one precedes and drives the other remains to be
501 investigated.

502 Whatever the case may be, the process by which the cells maintain the firing
503 output could, by itself, be a major source of stress for the cells. We do not know
504 whether the cells increase their conductance to compensate for the fast increase in
505 PICs or *vice versa*, but the result is the appearance of cells with both input
506 conductance and PIC amplitudes outside of the normal range (Figure 5A). The
507 increase in input conductance could be due to the insertion of more channels in the
508 membrane. However, direct measurements of soma sizes have revealed that pre-
509 symptomatic mutant cells are physically larger than controls (Shoenfeld et al., 2014;
510 Dukkipati et al., 2018). This increase in size, coupled with the larger calcium entry in
511 the cells due to the larger PICs (which are in part calcium-medicated (Li and
512 Bennett, 2003)), is bound to cause undue metabolic stress on those cells that are
513 outside of the normal range (Attwell and Laughlin, 2001), even though cells manage
514 to maintain a normal output. If we assume that all motoneurons experience the
515 same shift in their properties, then Fast Fatigable (FF) motoneurons, which are the
516 cells with the largest input conductance, and the largest PICs in normal conditions
517 (Lee and Heckman, 1998; Huh et al., 2017), are likely to be the cells that are the
518 further out of the normal range. This might explain why they are the most
519 vulnerable to ALS (Pun et al., 2006; Hegedus et al., 2007, 2008).

520 As the disease progresses, those large, vulnerable cells become the first
521 motoneurons that will embark on a degeneration pathway (Saxena et al., 2009,
522 2013; Martínez-Silva et al., 2018), and will lose their ability to fire repetitively
523 (Martínez-Silva et al., 2018). This early loss of the large cells is consistent with stress
524 induced by aberrantly large conductances and PICs. This loss is also likely the

525 primary reason why motoneurons appear to recover normal properties at late pre-
526 symptomatic stages. Nevertheless, it is probable that all motoneurons, regardless of
527 type, experience this form of stress. Interestingly, we observed that some of the
528 smallest motoneurons, which are the most resistant to the disease, appear to shrink
529 in the oldest animals (Figure 5C), consistent with anatomical observations (Kiernan
530 and Hudson, 1991; Dukkipati et al., 2018). At this point, it is unclear whether this
531 shrinkage is a pathological feature or a strong homeostatic effort by the surviving
532 motoneurons to counteract the stress generated by their initial hypertrophy.

533 ### Hyper-vigilant homeostasis

534 Mitchell and colleagues have recently performed meta-analyses of data obtained
535 from many studies on multiple cellular properties, which revealed patterns of
536 oscillations as the disease progressed, suggesting the existence of high feedback
537 gains for homeostatic processes (Mitchell and Lee, 2012; Irvin et al., 2015). Several
538 aspects of our results are consistent with this "hyper-vigilant" homeostasis
539 hypothesis. Similar oscillatory patterns are present in our results, as illustrated in
540 Figure 8. Although the cells are successful at maintaining their net excitability
541 constant, this is achieved at the cost of excessively high amplitudes for conductances
542 and PICs. These large amplitude changes lead to the appearance of groups of cells
543 that are first well above the normal range of properties, followed by an over-
544 reaction where some cells end up well below the normal range. This behavior fits
545 well with the "hyper-vigilant" model (Irvin et al., 2015), but a direct test of the
546 hyper-vigilant homeostasis hypothesis will require quantitative comparisons of the
547 responses of ALS and WT motoneurons to controlled homeostatic challenges.

548 ## Comparison with previous studies

549 Previous studies in adult SOD1 mice have suggested that spinal motoneurons
550 became hyperexcitable (Meehan et al., 2010; Jensen et al., 2020). The most recent
551 study uses the same SOD1(G93A) (albeit on a C57BL/6 genetic background) and
552 same anesthetics as the present study, but has focused on two fairly advanced time
553 points (~P75 and ~P115). They have observed an increase in input resistance
554 (decrease in input conductance) between WT and mSOD1 mice at both P75 and
555 P115. The increase at P115 is consistent with our results, and is probably due to the
556 loss of the largest motoneurons at this stage. However, we did not observe a
557 difference in resistance in our P60–90 group. The cause for this discrepancy
558 remains unknown, but it could suggest an earlier onset of cell death in their colony.
559 In their dataset, this decrease in conductance was associated with an apparent
560 hyperexcitability: the recruitment current was lower and the F-I curve was steeper.
561 However, their use of a low DCC switching rate (3 kHz, compared to 6–8 kHz used
562 here) may have distorted the firing properties of their cells and led to an
563 overestimation of their excitability (Manuel, 2020 in press).

564 We have previously studied the properties of motoneurons in the same
565 SOD1(G93A) mouse model of ALS (Delestrée et al., 2014; Martínez-Silva et al., 2018)
566 but have mainly focused on a short period just at the onset of denervations (P45–
567 55). Although that time point partly overlaps with the present young adult stage, we
568 had not detected differences in input conductances (Martínez-Silva et al., 2018).
569 This might be because the difference in input conductance is largest at earlier time
570 points (Figure 3). Indeed, the difference is gone at P60–90, and we did report an

571 increase in input conductance in an earlier series of experiments, which was more
572 pronounced in younger animals (Delestrée et al., 2014). Similarly, we did not detect
573 a difference in resting membrane potential in the Martínez-Silva et al. (2018) study.
574 Again, the discrepancy could be due to the difference in the distributions of the ages
575 of the animals studied. The precise reason for this difference remains, however,
576 unknown and warrants further study.

577 Since input conductance is dependent on motoneuron size (Burke, 1981;
578 Heckman and Enoka, 2012), our present results are consistent with anatomical
579 studies that have measured soma sizes in mSOD1 mice. In young adult animals,
580 motoneurons are markedly larger in mSOD1 mice compared to WT animals
581 (particularly in males)(Shoenfeld et al., 2014; Dukkipati et al., 2018). At
582 symptomatic stages, however, the situation is reversed and the remaining
583 motoneurons appear to have shrunk below the size of the smallest motoneurons in
584 WT mice (Dukkipati et al., 2018).

585 In the present study, we recorded only 13 motoneurons out of 103 (7/50 WT and
586 6/53 mSOD1) that were unable to fire repetitively, contrary to our previous study
587 where we showed that a large proportion of vulnerable motoneurons became
588 hypoexcitable before the onset of denervation (P45–55, Martínez-Silva et al., 2018).
589 This discrepancy could be explained by the experimental constraints of the present
590 study. Indeed, obtaining stable voltage-clamp recordings mice in vivo is quite a
591 challenge, requiring electrodes able to pass substantial amounts of current and
592 motoneuron able to withstand the protocol. Since we have only included for analysis
593 cells in which both the voltage-clamp and current-clamp protocols were completed

594 successfully, we hypothesize that we may have biased our sample towards the
595 healthiest cells that have yet to take the path of degeneration.

596 ## Limitations

597 The results presented here have been collected on the SOD1(G93A) mouse model
598 of ALS, a model that has attracted criticisms due to it being an overexpression
599 model, and its failure to bring seemingly promising therapies to the clinic (Philips
600 and Rothstein, 2015). Nevertheless, some parallel with other studies suggests that
601 our results could be extended to other models. First, Meehan et al. (2010) have
602 studied an unrelated mSOD1(G127X) model and have shown that although the net
603 excitability of the motoneurons was not affected by the mutation, there were
604 nonetheless signs of increased PICs in these motoneurons. Second, we observed
605 that, in late symptomatic animals, some cells exhibited a very small input
606 conductance, well below the normal range at this age, suggesting that these cells
607 actually shrank. This observation matches morphological measurements in mSOD1
608 mice (Dukkipati et al., 2018), but also observations from sporadic human patients
609 (Kiernan and Hudson, 1991).

610 We demonstrated a remarkably successful homeostatic control of motoneuron
611 firing, that we can attribute to commensurate changes in PICs and input
612 conductance. However, it is likely that other currents are also implicated in this
613 process (Marder and Goaillard, 2006). Limitations inherent to in vivo
614 electrophysiology prevent us from isolating many different currents and further in
615 vitro investigations in adults (Jiang and Heckman, 2006; Mitra and Brownstone,

616 2011; Jiang et al., 2017; Bhumbra and Beato, 2018) are warranted to shed more light
617 on the panoply of channels involved in this process.

618 ### Conclusion

619 Overall, our results show homeostasis for net excitability in mutant SOD1
620 motoneurons is remarkably strong in the presymptomatic state. This success
621 however comes at a cost of large compensatory changes in basic electrical
622 properties. These results support the hypothesis that ALS is not due to a single
623 specific root cause but instead caused by an inherent instability at the system-level
624 (Mitchell and Lee, 2012), possibly caused by a "hyper-vigilant" homeostatic system
625 in motoneurons. Initial perturbations in the electrical properties of motoneurons
626 would be overcompensated for, leading to new sources of stress, which, in turn,
627 would be overcorrected, and so forth until the metabolic burden becomes too high
628 to sustain for the motoneuron. FF motoneurons have higher metabolic needs (Le
629 Masson et al., 2014) and lower calcium-buffering capabilities (Grosskreutz et al.,
630 2010) in the first place, which make them particularly vulnerable to this vicious
631 cycle.

632 ## Data availability

633 Data files and a computational notebook allowing reproducing the analysis and
634 figures of this article are provided at the URL:
635 https://doi.org/10.5281/zenodo.3831946

636 ## References

637 Attwell D, Laughlin SB (2001) An Energy Budget for Signaling in the Grey Matter of
638 the Brain. J Cereb Blood Flow Metab 21:1133–1145 DOI: 10.1097/00004647-
639 200110000-00001.
640 Bączyk M, Ouali Alami N, Delestrée N, Martinot C, Tang L, Commisso B, Bayer D,
641 Doisne N, Frankel W, Manuel M, Roselli F, Zytnicki D (2020) Synaptic
642 restoration by cAMP/PKA drives activity-dependent neuroprotection to
643 motoneurons in ALS. J Exp Med 217 DOI: 10.1084/jem.20191734.
644 Bernard C (2019) Changing the Way We Report, Interpret, and Discuss Our Results
645 to Rebuild Trust in Our Research. eNeuro 6 DOI: 10.1523/ENEURO.0259-
646 19.2019.
647 Bhumbra GS, Beato M (2018) Recurrent excitation between motoneurones
648 propagates across segments and is purely glutamatergic. PLOS Biol
649 16:e2003586 DOI: 10.1371/journal.pbio.2003586.
650 Brownstone RM, Lancelin C (2018) Escape from homeostasis: spinal microcircuits
651 and progression of amyotrophic lateral sclerosis. J Neurophysiol 119:1782–
652 1794 DOI: 10.1152/JN.00331.2017.
653 Burke RE (1981) Motor units: anatomy, physiology, and functional organization. In:
654 Handbook of physiology. The nervous system. Motor control., pp 345–422.
655 American Physiological Society.
656 Cumming G (2012) Understanding the new statistics: effect sizes, confidence
657 intervals, and meta-analysis. New York: Routledge, Taylor & Francis Group.
658 Delestrée N, Manuel M, Iglesias C, Elbasiouny SM, Heckman CJ, Zytnicki D (2014)
659 Adult spinal motoneurones are not hyperexcitable in a mouse model of
660 inherited amyotrophic lateral sclerosis. J Physiol 592:1687–1703 DOI:
661 10.1113/JPHYSIOL.2013.265843.
662 Dukkipati SS, Garrett TL, Elbasiouny SM (2018) The vulnerability of spinal
663 motoneurons and soma size plasticity in a mouse model of amyotrophic lateral
664 sclerosis. J Physiol 596:1723–1745 DOI: 10.1113/JP275498.
665 Grosskreutz J, van den Bosch L, Keller BU (2010) Calcium dysregulation in
666 amyotrophic lateral sclerosis. Cell Calcium 47:165–174 DOI:
667 10.1016/j.ceca.2009.12.002.
668 Heckman CJ, Enoka RM (2012) Motor Unit. Compr Physiol 2:2629–2682 DOI:
669 10.1002/cphy.c100087.
670 Hedges LV (2016) Distribution Theory for Glass's Estimator of Effect size and
671 Related Estimators: J Educ Stat DOI: 10.3102/10769986006002107.
672 Hegedus J, Putman CT, Gordon T (2007) Time course of preferential motor unit loss
673 in the SOD1 G93A mouse model of amyotrophic lateral sclerosis. Neurobiol Dis
674 28:154–164 DOI: 10.1016/j.nbd.2007.07.003.
675 Hegedus J, Putman CT, Tyreman N, Gordon T (2008) Preferential motor unit loss in
676 the SOD1 G93A transgenic mouse model of amyotrophic lateral sclerosis. J
677 Physiol 586:3337–3351 DOI: 10.1113/jphysiol.2007.149286.

678 Herculano-Houzel S (2011) Scaling of Brain Metabolism with a Fixed Energy Budget
679 per Neuron: Implications for Neuronal Activity, Plasticity and Evolution. PLoS
680 ONE 6 DOI: 10.1371/journal.pone.0017514.
681 Ho J, Tumkaya T, Aryal S, Choi H, Claridge-Chang A (2019) Moving beyond P values:
682 data analysis with estimation graphics. Nat Methods 16:565–566 DOI:
683 10.1038/s41592-019-0470-3.
684 Howarth C, Gleeson P, Attwell D (2012) Updated Energy Budgets for Neural
685 Computation in the Neocortex and Cerebellum. J Cereb Blood Flow Metab
686 32:1222–1232 DOI: 10.1038/jcbfm.2012.35.
687 Huh S, Siripuram R, Lee RH, Turkin VV, O'Neill D, Hamm TM, Heckman CJ, Manuel M
688 (2017) PICs in motoneurons do not scale with the size of the animal: a possible
689 mechanism for faster speed of muscle contraction in smaller species. J
690 Neurophysiol 118:93–102 DOI: 10.1152/JN.00045.2017.
691 Hunter JD (2007) Matplotlib: A 2D Graphics Environment. Comput Sci Eng 9:90–95
692 DOI: 10.1109/MCSE.2007.55.
693 Ilieva H, Polymenidou M, Cleveland DW (2009) Non-cell autonomous toxicity in
694 neurodegenerative disorders: ALS and beyond. J Cell Biol 187:761–772 DOI:
695 10.1083/jcb.200908164.
696 Irvin CW, Kim RB, Mitchell CS (2015) Seeking homeostasis: temporal trends in
697 respiration, oxidation, and calcium in SOD1 G93A Amyotrophic Lateral
698 Sclerosis mice. Front Cell Neurosci 9:248 DOI: 10.3389/FNCEL.2015.00248.
699 Jensen DB, Kadlecova M, Allodi I, Meehan CF (2020) Spinal motoneurones are
700 intrinsically more responsive in the adult G93A SOD1 mouse model of
701 amyotrophic lateral sclerosis. J Physiol 598:4385–4403 DOI:
702 10.1113/JP280097.
703 Jiang MC, Adimula A, Birch D, Heckman CJ (2017) Hyperexcitability in synaptic and
704 firing activities of spinal motoneurons in an adult mouse model of
705 amyotrophic lateral sclerosis. Neuroscience 362:33–46 DOI:
706 10.1016/j.neuroscience.2017.08.041.
707 Jiang MC, Heckman CJ (2006) In vitro sacral cord preparation and motoneuron
708 recording from adult mice. J Neurosci Off J Soc Neurosci 156:31–36.
709 Johnson MD, Heckman CJ (2010) Interactions between focused synaptic inputs and
710 diffuse neuromodulation in the spinal cord. Ann N Y Acad Sci 1198:35–41 DOI:
711 10.1111/J.1749-6632.2010.05430.X.
712 Kanning KC, Kaplan A, Henderson CE (2009) Motor neuron diversity in development
713 and disease. Annu Rev Neurosci 33:409–440.
714 Kiernan JA, Hudson AJ (1991) Changes in Sizes of Cortical and Lower Motor Neurons
715 in Amyotrophic Lateral Sclerosis. Brain 114:843–853 DOI:
716 10.1093/brain/114.2.843.
717 Kim J, Hughes EG, Shetty AS, Arlotta P, Goff LA, Bergles DE, Brown SP (2017)
718 Changes in the Excitability of Neocortical Neurons in a Mouse Model of
719 Amyotrophic Lateral Sclerosis Are Not Specific to Corticospinal Neurons and
720 Are Modulated by Advancing Disease. J Neurosci Off J Soc Neurosci 37:9037–
721 9053 DOI: 10.1523/JNEUROSCI.0811-17.2017.
722 Kuo JJ, Schonewille M, Siddique T, Schults ANA, Fu R, Bär PR, Anelli R, Heckman CJ,
723 Kroese ABA (2004) Hyperexcitability of cultured spinal motoneurons from

presymptomatic ALS mice. J Neurophysiol 91:571–575 DOI: 10.1152/jn.00665.2003.

Lalancette-Hebert M, Sharma A, Lyashchenko AK, Shneider NA (2016) Gamma motor neurons survive and exacerbate alpha motor neuron degeneration in ALS. Proc Natl Acad Sci U S A 113:E8316–E8325 DOI: 10.1073/pnas.1605210113.

Le Masson G, Przedborski S, Abbott LF (2014) A Computational Model of Motor Neuron Degeneration. Neuron 83:758–760 DOI: 10.1016/j.neuron.2014.07.001.

Lee RH, Heckman CJ (1998) Bistability in spinal motoneurons in vivo: systematic variations in persistent inward currents. J Neurophysiol 80:583–593.

Leitner M, Menzies S, Lutz C (2009) Working with ALS Mice. The Jackson Laboratory.

Leroy F, Lamotte d'Incamps B, Imhoff-Manuel RD, Zytnicki D (2014) Early intrinsic hyperexcitability does not contribute to motoneuron degeneration in amyotrophic lateral sclerosis. eLife 3 DOI: 10.7554/eLife.04046.

Li Y, Bennett DJ (2003) Persistent sodium and calcium currents cause plateau potentials in motoneurons of chronic spinal rats. J Neurophysiol 90:857–869.

Makin TR, Orban de Xivry J-J (2019) Ten common statistical mistakes to watch out for when writing or reviewing a manuscript Rodgers P, Parsons N, Holmes N, eds. eLife 8:e48175 DOI: 10.7554/eLife.48175.

Manuel M (2020) Sub-optimal Discontinuous Current-Clamp switching rates lead to deceptive mouse neuronal firing. bioRxiv:2020.08.13.250134 DOI: 10.1101/2020.08.13.250134.

Manuel M, Heckman CJ (2011) Adult mouse motor units develop almost all of their force in the subprimary range: a new all-or-none strategy for force recruitment? J Neurosci 31:15188–15194 DOI: 10.1523/JNEUROSCI.2893-11.2011.

Manuel M, Iglesias C, Donnet M, Leroy F, Heckman CJ, Zytnicki D (2009) Fast kinetics, high-frequency oscillations, and subprimary firing range in adult mouse spinal motoneurons. J Neurosci 29:11246–11256 DOI: 10.1523/JNEUROSCI.3260-09.2009.

Marder E, Goaillard J-M (2006) Variability, compensation and homeostasis in neuron and network function. Nat Rev Neurosci 7:563–574 DOI: 10.1038/nrn1949.

Martin E, Cazenave W, Cattaert D, Branchereau P (2013) Embryonic alteration of motoneuronal morphology induces hyperexcitability in the mouse model of amyotrophic lateral sclerosis. Neurobiol Dis 54:116–126 DOI: 10.1016/j.nbd.2013.02.011.

Martínez-Silva M de L, Imhoff-Manuel RD, Sharma A, Heckman C, Shneider NA, Roselli F, Zytnicki D, Manuel M (2018) Hypoexcitability precedes denervation in the large fast-contracting motor units in two unrelated mouse models of ALS Rubin LL, ed. eLife 7:e30955 DOI: 10.7554/ELIFE.30955.

McKinney W (2011) pandas: a foundational Python library for data analysis and statistics. Python High Perform Sci Comput 14.

769 Meehan CF, Moldovan M, Marklund SL, Graffmo KS, Nielsen JB, Hultborn H (2010)
770 Intrinsic properties of lumbar motor neurones in the adult G127insTGGG
771 superoxide dismutase-1 mutant mouse in vivo: evidence for increased
772 persistent inward currents. Acta Physiol Oxf Engl 200:361–376 DOI:
773 10.1111/j.1748-1716.2010.02188.x.
774 Michel MC, Murphy TJ, Motulsky HJ (2020) New Author Guidelines for Displaying
775 Data and Reporting Data Analysis and Statistical Methods in Experimental
776 Biology. Mol Pharmacol 97:49–60 DOI: 10.1124/mol.119.118927.
777 Mitchell CS, Lee RH (2012) Dynamic Meta-Analysis as a Therapeutic Prediction Tool
778 for Amyotrophic Lateral Sclerosis. In: Amyotrophic Lateral Sclerosis (Maurer
779 M, ed). InTech. DOI: 10.5772/32384.
780 Mitra P, Brownstone RM (2011) An in vitro spinal cord slice preparation for
781 recording from lumbar motoneurons of the adult mouse. J Neurophysiol
782 107:728–741 DOI: 10.1152/JN.00558.2011.
783 O'Leary T, Rossum MCW van, Wyllie DJA (2010) Homeostasis of intrinsic excitability
784 in hippocampal neurones: dynamics and mechanism of the response to chronic
785 depolarization. J Physiol 588:157–170 DOI: 10.1113/jphysiol.2009.181024.
786 O'Leary T, Wyllie DJA (2011) Neuronal homeostasis: time for a change? J Physiol
787 589:4811–4826 DOI: 10.1113/jphysiol.2011.210179.
788 Pedregosa F, Varoquaux G, Gramfort A, Michel V, Thirion B, Grisel O, Blondel M,
789 Prettenhofer P, Weiss R, Dubourg V, Vanderplas J, Passos A, Cournapeau D,
790 Brucher M, Perrot M, Duchesnay E (2011) Scikit-learn: Machine Learning in
791 Python. J Mach Learn Res 12:2825–2830.
792 Philips T, Rothstein JD (2015) Rodent Models of Amyotrophic Lateral Sclerosis. Curr
793 Protoc Pharmacol Editor Board SJ Enna Ed--Chief Al 69:5.67.1-5.67.21 DOI:
794 10.1002/0471141755.ph0567s69.
795 Pieri M, Carunchio I, Curcio L, Mercuri NB, Zona C (2009) Increased persistent
796 sodium current determines cortical hyperexcitability in a genetic model of
797 amyotrophic lateral sclerosis. Exp Neurol 215:368–379 DOI:
798 10.1016/j.expneurol.2008.11.002.
799 Pun S, Santos AF, Saxena S, Xu L, Caroni P (2006) Selective vulnerability and pruning
800 of phasic motoneuron axons in motoneuron disease alleviated by CNTF. Nat
801 Neurosci 9:408–419 DOI: 10.1038/nn1653.
802 Quinlan KA, Schuster JE, Fu R, Siddique T, Heckman CJ (2011) Altered postnatal
803 maturation of electrical properties in spinal motoneurons in a mouse model of
804 amyotrophic lateral sclerosis. J Physiol 589:2245–2260.
805 Rolfe DF, Brown GC (1997) Cellular energy utilization and molecular origin of
806 standard metabolic rate in mammals. Physiol Rev 77:731–758 DOI:
807 10.1152/physrev.1997.77.3.731.
808 Rosen DR, Siddique T, Patterson D, Figlewicz DA, Sapp P, Hentati A, Donaldson D,
809 Goto J, O'Regan JP, Deng H-X (1993) Mutations in Cu/Zn superoxide dismutase
810 gene are associated with familial amyotrophic lateral sclerosis. Nature 362:59–
811 62 DOI: 10.1038/362059a0.
812 Saxena S, Cabuy E, Caroni P (2009) A role for motoneuron subtype-selective ER
813 stress in disease manifestations of FALS mice. Nat Neurosci 12:627–636 DOI:
814 10.1038/nn.2297.

Saxena S, Roselli F, Singh K, Leptien K, Julien J, Gros-louis F, Caroni P (2013) Neuroprotection through Excitability and mTOR Required in ALS Motoneurons to Delay Disease and Extend Survival. Neuron 80:80–96 DOI: 10.1016/j.neuron.2013.07.027.

Seabold S, Perktold J (2010) statsmodels: Econometric and statistical modeling with python. In: 9th Python in Science Conference DOI: 10.25080/Majora-92bf1922-011.

Sekerli M, Del Negro CA, Lee RH, Butera RJ (2004) Estimating action potential thresholds from neuronal time-series: new metrics and evaluation of methodologies. IEEE Trans Biomed Eng 51:1665–1672 DOI: 10.1109/TBME.2004.827531.

Shoenfeld L, Westenbroek RE, Fisher E, Quinlan K a, Tysseling VM, Powers RK, Heckman CJ, Binder MD (2014) Soma size and Cav1.3 channel expression in vulnerable and resistant motoneuron populations of the SOD1G93A mouse model of ALS. Physiol Rep 2:e12113 DOI: 10.14814/phy2.12113.

Turrigiano G, Abbott LF, Marder E (1994) Activity-dependent changes in the intrinsic properties of cultured neurons. Science 264:974–977 DOI: 10.1126/science.8178157.

van Zundert B, Peuscher MH, Hynynen M, Chen A, Neve RL, Brown RH, Constantine-Paton M, Bellingham MC (2008) Neonatal neuronal circuitry shows hyperexcitable disturbance in a mouse model of the adult-onset neurodegenerative disease amyotrophic lateral sclerosis. J Neurosci Off J Soc Neurosci 28:10864–10874 DOI: 10.1523/JNEUROSCI.1340-08.2008.

Virtanen P et al. (2020) SciPy 1.0: fundamental algorithms for scientific computing in Python. Nat Methods:1–12 DOI: 10.1038/s41592-019-0686-2.

Waskom M et al. (2020) mwaskom/seaborn: v0.10.0 (January 2020). Zenodo. DOI: 10.5281/zenodo.3629446.

Wasserstein RL, Schirm AL, Lazar NA (2019) Moving to a World Beyond "p < 0.05." Am Stat 73:1–19 DOI: 10.1080/00031305.2019.1583913.

Welch BL (1947) The generalisation of student's problems when several different population variances are involved. Biometrika 34:28–35 DOI: 10.1093/biomet/34.1-2.28.

Figure legends

Figure 1: PIC amplitude is larger is young adult mSOD1 mice

A. Example of a PIC recording from a P43 WT mouse. The green bottom trace is the ascending part of the voltage ramp. The top blue trace is the raw current. The dashed line shows the leak current estimated by fitting a straight line in the subthreshold potential region, and which is used to measure the input conductance

854 of the cell. The leak-subtracted current trace is obtained by subtracting the leak
855 current from the raw current trace. The dash-dotted lines show some of the
856 measurements: *PIC amp.*: PIC amplitude, measured at the point of largest deflection
857 on the leak-subtracted trace; V_{onset}: voltage at which the PICs start to activate; V_{peak}:
858 voltage at which PICs reach their maximum. **B.** Example of a PIC recording from a
859 P35 mSOD1 mouse. Same organization as in A. **C.** Plot of the amplitude of the PICs
860 (in nA) vs. age in WT (blue square) and mSOD1 mice (red diamonds). The solid lines
861 correspond to the linear regression lines with 95% confidence intervals (shaded
862 areas). WT: slope=0.12 nA/week 95%CI[−0.068–0.32], r^2=0.034 (p=0.2); SOD1:
863 slope=−0.45 nA/week 95%CI[−0.64–−0.25], r^2=0.29 (p=3.4e−05). **D**. Breakdown of
864 the difference in PIC amplitude between WT and mSOD1 animals by age groups.
865 P30–60 WT: 2.30±2.17 nA, N=19 vs. mSOD1: 6.73±3.28 nA, N=15; g=1.59
866 95%CI[0.63–2.45]; t(32)=−4.50, p=0.00016. P60–90 WT: 2.47±1.69 nA, N=16 vs.
867 mSOD1: 2.75±2.40 nA, N=24; g=0.12 95%CI[−0.53–0.65]; t(38)=−0.42, p=0.67. P90–
868 120 WT: 4.12±3.69 nA, N=15 vs. mSOD1: 1.90±1.78 nA, N=14; g=−0.74
869 95%CI[−1.26–0.01]; t(27)=2.08, p=0.05. **E.** Evolution of the membrane potential at
870 which the PICs start to activate (PIC onset voltage) vs. age. WT:
871 slope=−0.33 mV/week 95%CI[−0.77–0.11], r^2=0.045 (p=0.14). SOD1:
872 slope=0.91 mV/week 95%CI[0.41–1.4], r^2=0.21 (p=0.00063). **F.** Evolution of the
873 membrane potential at which the PICs reach their peak (PIC peak voltage) vs. age.
874 WT: slope=−0.29 mV/week 95%CI[−0.73–0.16], r^2=0.034 (p=0.2). SOD1:
875 slope=0.68 mV/week 95%CI[0.28–1.1], r^2=0.18 (p=0.0014). **G.** Evolution of the
876 voltage threshold for spiking (measure in current-clamp mode) vs. age. WT:

877 slope=−0.14 mV/week 95%CI[−0.57–0.28], r^2=0.0096 (p=0.5). SOD1:

878 slope=0.77 mV/week 95%CI[0.34–1.2], r^2=0.23 (p=0.0007).

879 **Figure 2. Mutant motoneurons are not hyperexcitable**

880 **A.** Example of the response of a P43 WT mouse (same motoneuron as in Figure

881 1A) to a triangular ramp of current. From bottom to top, traces are: injected current,

882 membrane potential, and instantaneous firing frequency. The dash-dotted lines

883 show some of the measurements: $I_{recruit.}$: current intensity at which the motoneuron

884 starts to fire; $I_{derecruit.}$: de-recruitment current; ΔI: difference between the de-

885 recruitment and recruitment currents; $I_{trans.\ SPR/PR}$: the current at the transition

886 between sub-primary range and primary range; *F-I gain*: slope of the linear fit of the

887 firing frequency in the primary range; ΔF: difference between the instantaneous

888 firing frequency at de-recruitment and recruitment; V_{th}: voltage threshold for

889 spiking measured on the first spike of the ramp. **B.** Example of the response of a P35

890 mSOD1 mouse (same motoneuron as in Figure 1B). Same organization as in A. **C.**

891 Plot of the current intensity required for eliciting the first spike on a triangular ramp

892 of current in WT (blue squares) and mSOD1 motoneurons (red diamonds). WT:

893 slope=0.1 nA/week 95%CI[−0.11–0.31], r^2=0.019 (p=0.34). SOD1:

894 slope=−0.35 nA/week 95%CI[−0.56–−0.14], r^2=0.2 (p=0.0019). **D.** Breakdown of the

895 difference in recruitment current between WT and mSOD1 motoneurons in each of

896 the age groups. In young adult and presymptomatic mice, mutant motoneurons

897 require the same amount of current than WT motoneuron to fire, P30–60 WT:

898 4.73±3.14 nA, N=19 vs. mSOD1: 6.21±2.51 nA, N=14; g=0.50 95%CI[−0.24–1.24];

899 t(31)=−1.51, p=0.14. P60–90 WT: 5.28±2.64 nA, N=16 vs. mSOD1: 4.53±3.38 nA,

900 N=20; g=−0.24 95%CI[−0.93–0.41]; t(34)=0.75, p=0.46. At the symptomatic stages
901 (P90–120), mutant motoneurons exhibit a lower current threshold for firing (WT:
902 5.43±3.07 nA, N=15 vs. mSOD1: 2.19±1.56 nA, N=13; g=−1.26 95%CI[−1.95–−0.47];
903 t(26)=3.59, p=0.0017), compatible with the loss of the least excitable cells. **E.** The
904 slope of the F-I relationship, measured over the primary range, is not affected by the
905 mutation, regardless of the age of the animals. WT: slope=−0.13 Hz/nA/week
906 95%CI[−0.65–0.38], r^2=0.011 (p=0.6). SOD1: slope=0.27 Hz/nA/week 95%CI[−0.23–
907 0.77], r^2=0.028 (p=0.28). **F.** Breakdown of the difference between WT and mSOD1
908 motoneurons by age group: P30–60 WT: 9.3±3.6 Hz/nA, N=10 vs. mSOD1:
909 8.3±3.4 Hz/nA, N=14; g=−0.28 95%CI[−1.10–0.64]; t(22)=0.69, p=0.5. P60–90 WT:
910 12.2±7.3 Hz/nA, N=8 vs. mSOD1: 10.3±6.4 Hz/nA, N=16; g=−0.27 95%CI[−1.22–
911 0.54]; t(22)=0.62, p=0.54. P90–120 WT: 8.0±3.2 Hz/nA, N=10 vs. mSOD1:
912 10.8±9.1 Hz/nA, N=13; g=0.38 95%CI[−0.43–0.93]; t(21)=−1.04, p=0.31.

913 **Figure 3: Young mutant motoneurons have an aberrantly large input**
914 **conductance**

915 **A.** Plot of the motoneuron input conductance vs. age in WT (blue squares) and
916 mSOD1 (red diamonds) animals. The solid lines correspond to the linear regression
917 lines with 95% confidence intervals (shaded areas). WT slope=0.018 μS/week
918 95%CI[0.0061–0.029], r^2=0.16 (p=0.0035) ; SOD1 slope=−0.041 μS/week
919 95%CI[−0.052–−0.03], r^2=0.53 (p=6.1e−10).) **B.** Breakdown of the difference in
920 input conductance between WT and mSOD1 animals by age groups. P30–60 WT:
921 0.42±0.16 μS, N=19 vs. mSOD1: 0.72±0.18 μS, N=15; g=1.73 95%CI[0.92–2.41];
922 t(32)=−5.06, p=2.2e−05. P60–90 WT: 0.46±0.16 μS, N=16 vs. mSOD1: 0.42±0.15 μS,

923 N=24; g=−0.28 95%CI[−0.96–0.37]; t(38)=0.88, p=0.39. P90–120 WT: 0.60±0.15 μS,
924 N=15 vs. mSOD1: 0.33±0.13 μS, N=14; g=−1.85 95%CI[−2.57–−1.16]; t(27)=5.16,
925 p=2.1e−05.

926 **Figure 4. The resting membrane potential of young adult mutant mice is**
927 **hyperpolarized**

928 **A.** Plot of the motoneuron resting membrane potential vs. age in WT (blue
929 squares) and mSOD1 (red diamonds) animals. The solid lines correspond to the
930 linear regression lines with 95% confidence intervals (shaded areas). WT:
931 slope=−0.068 mV/week 95%CI[−0.52–0.38], r^2=0.0019 (p=0.76). SOD1:
932 slope=0.81 mV/week 95%CI[0.31–1.3], r^2=0.18 (p=0.0022). **B.** Breakdown of the
933 difference in resting membrane potential between WT and mSOD1 animals by age
934 groups. P30–60 WT: −62.38±5.52 mV, N=19 vs. mSOD1: −71.45±8.78 mV, N=15;
935 g=−1.24 95%CI[−2.13–−0.23]; t(32)=3.49, p=0.002. P60–90 WT: −60.98±5.35 mV,
936 N=16 vs. mSOD1: −66.18±5.63 mV, N=22; g=−0.92 95%CI[−1.54–−0.18]; t(36)=2.89,
937 p=0.0067. P90–120 WT: −64.71±7.42 mV, N=15 vs. mSOD1: −61.99±5.43 mV, N=13;
938 g=0.40 95%CI[−0.35–1.10]; t(26)=−1.12, p=0.27.

939 **Figure 5. Some motoneurons exhibit properties outside of the normal range**

940 **A.** Plot of the PIC amplitude vs. the input conductance of young adult
941 motoneurons (P30–60) in WT (blue squares) and mSOD1 (red diamonds) animals.
942 The grey line is the best linear fit ± 95% confidence interval (shaded area) for both
943 samples. Slope=7.7 mV 95%CI[2.6–12.7], r^2=0.55 (p=0.004). The marginal plots
944 indicate the kernel density estimation of the distributions of the values in the two
945 populations. The ‡ symbol points to the fraction of the mSOD1 population that is

946 outside the range of the WT population. **B.** Same as A for the presymptomatic age
947 range P60–90. Slope=5.4 mV 95%CI[1.1–9.8], r^2=0.15 (p=0.016). **C.** Same as A for
948 the symptomatic age range P90–120. Slope=7.0 mV 95%CI[−0.8–14.9], r^2=0.23
949 (p=0.078).

950 **Figure 6: Some cells are hypoexcitable and cannot fire repetitively**

951 **A.** Example of an mSOD1 motoneuron (from a P88 mouse) that is unable to fire
952 repetitively in response to a triangular ramp of current. Top trace: membrane
953 potential, bottom trace: injected current. **B.** This same motoneuron was
954 nevertheless able to generate a single full-height action potential in response to a
955 square pulse of current. Same organization as in A. **C.** Voltage-clamp measurement
956 of the PICs in this same motoneuron. Traces are (from top to bottom), leak current
957 (dashed line), raw current (blue), leak-subtracted current (red) and voltage
958 command (green). **D.** Non-firing motoneurons had a similar input conductance
959 compared to motoneurons capable of firing repetitively. Firing: 0.49±0.22 μS, N=47
960 vs. non-firing: 0.38±0.20 μS, N=6; g=−0.54 95%CI[−1.11–0.50]; t(51)=1.36, p=0.22 **E.**
961 Non-firing motoneurons had much smaller PICs than motoneurons able to fire
962 repetitively. Firing: Firing: 4.04±3.18 nA, N=47 vs. non-firing: 0.60±0.49 nA, N=6;
963 g=−1.12 95%CI[−1.42−−0.86]; t(51)=6.81, p=1.3e−08 **F.** Non-firing motoneurons
964 appear earlier in mSOD1 animals compared to WT animals. WT: 100±16 days old,
965 N=7 vs. SOD1: 75±23 days old, N=6; g=−1.20 95%CI[−2.06–0.01]; t(11)=2.24,
966 p=0.053.

967 **Figure 7. Overview of the change in principal components over time.**

968 **A_{1-3}.** Plot of the three first principal components vs. age in WT (blue squares) and
969 mSOD1 motoneurons (red diamonds). The solid lines correspond to the linear
970 regression lines with 95% confidence intervals (shaded areas). **B.** Heatmap showing
971 the correlation coefficient between each principal component (columns) and the
972 features (rows) shown on the right. Correlation coefficients are color-coded from
973 dark blue (r=−1) to dark red (r=+1). **C.** Summary of the evolution of the difference
974 between WT and mSOD1 motoneurons (quantified by the effect size Hedges' g) for
975 each of the features and each of the time points considered. The features are
976 ordered by the size of the effect of the mutation in the P30–60 age group. On each
977 row, the dashed line represents an effect size of zero. Scale bar: 2 units.

978 **Figure 8: summary of the changes in motoneuron properties over time**

979 Schematic representation of the changes in four key electrophysiological
980 properties over time. The dots represent the effect size (Hedges' g) and the vertical
981 bars show the 95%CI around g. The thin lines are cubic splines interpolation of the
982 data over time. The points have been slightly staggered so that the vertical bars do
983 not occlude each other. †Data from embryonic motoneurons are from Martin et al.
984 (2013). These authors did not measure PICs in embryonic motoneurons. Kuo et al.
985 (2004) did measure PICs, but their embryonic motoneurons were cultured for 10–
986 30 days in vitro, and their development stage is therefore uncertain. ‡Data from
987 neonates (P0–5 and P6–12) are from Quinlan et al. (2011).

988 **Table 1: summary of the properties of the motoneurons, broken down by age**
989 **range**

990 The table shows the various properties that were measured in each motoneuron.
991 The rows are sorted in descending order of effect size at P30–60. WT and mSOD1
992 columns show mean values ± standard deviation, with the 95%CI around the mean
993 below. The "Mean diff." column shows the mean difference between mSOD1 and WT
994 population, with 95% CI and the result of Welch's test (for information). The
995 "Hedges' *g*" column shows the effect size and its 95%CI below.

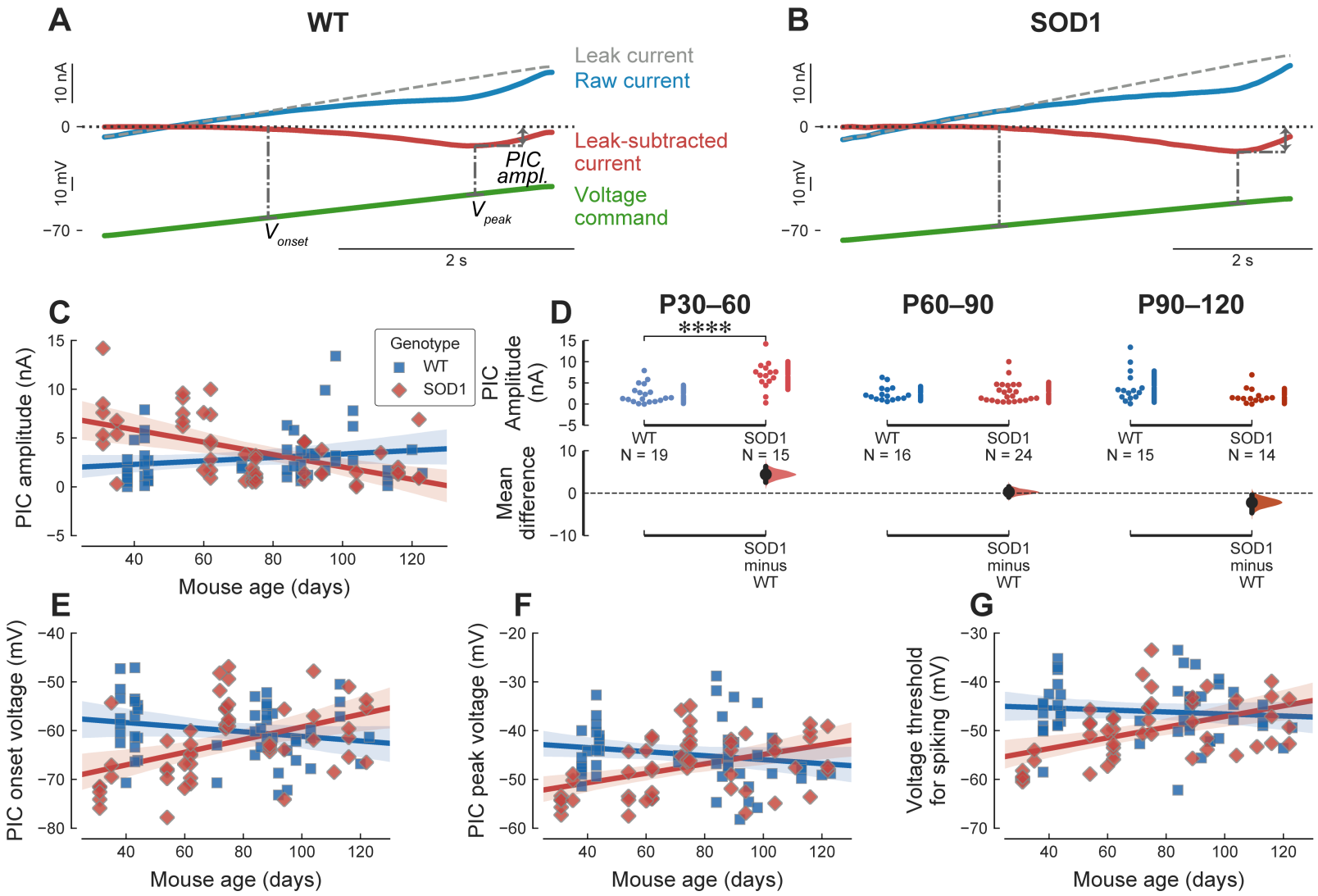
A
WT
B
SOD1
Leak current
Raw current
Leak-subtracted current
Voltage command
PIC ampl.
V_{onset}
V_{peak}
10 nA
10 mV
0
−70
2 s
C
PIC amplitude (nA)
Mouse age (days)
Genotype
WT
SOD1
D
P30–60
P60–90
P90–120
****
PIC Amplitude (nA)
Mean difference
WT N = 19
SOD1 N = 15
WT N = 16
SOD1 N = 24
WT N = 15
SOD1 N = 14
SOD1 minus WT
E
PIC onset voltage (mV)
F
PIC peak voltage (mV)
G
Voltage threshold for spiking (mV)

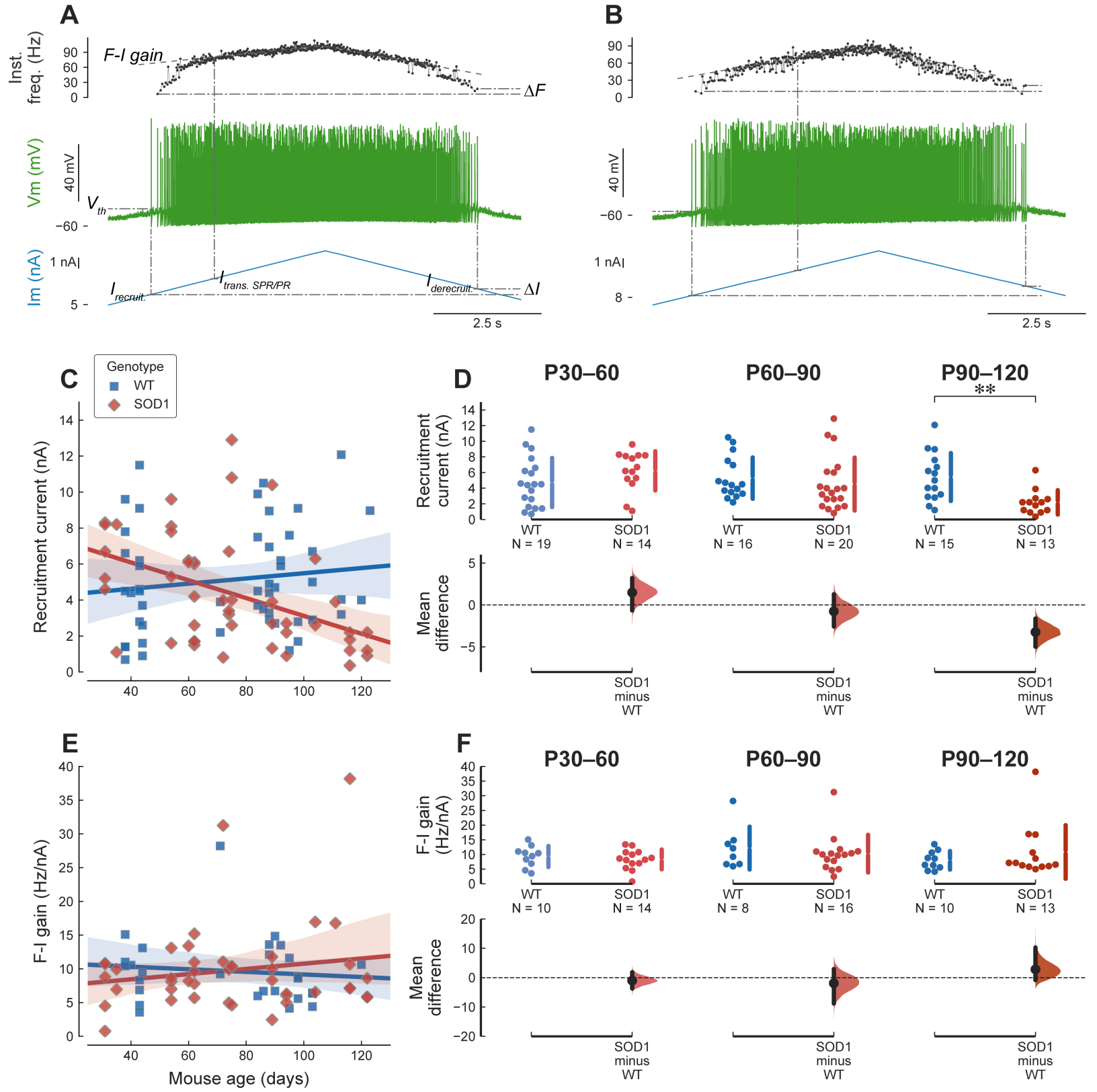
A
Inst. freq. (Hz)
F-I gain
ΔF
Vm (mV)
40 mV
V th
−60
Im (nA)
1 nA
I recruit.
I trans. SPR/PR
I derecruit.
ΔI
5
2.5 s
B
90
60
30
0
40 mV
−60
1 nA
8
2.5 s
C
Genotype
WT
SOD1
Recruitment current (nA)
D
P30–60
P60–90
P90–120
**
Recruitment current (nA)
WT N = 19
SOD1 N = 14
WT N = 16
SOD1 N = 20
WT N = 15
SOD1 N = 13
Mean difference
SOD1 minus WT
E
F-I gain (Hz/nA)
Mouse age (days)
F
P30–60
P60–90
P90–120
F-I gain (Hz/nA)
WT N = 10
SOD1 N = 14
WT N = 8
SOD1 N = 16
WT N = 10
SOD1 N = 13
Mean difference
SOD1 minus WT

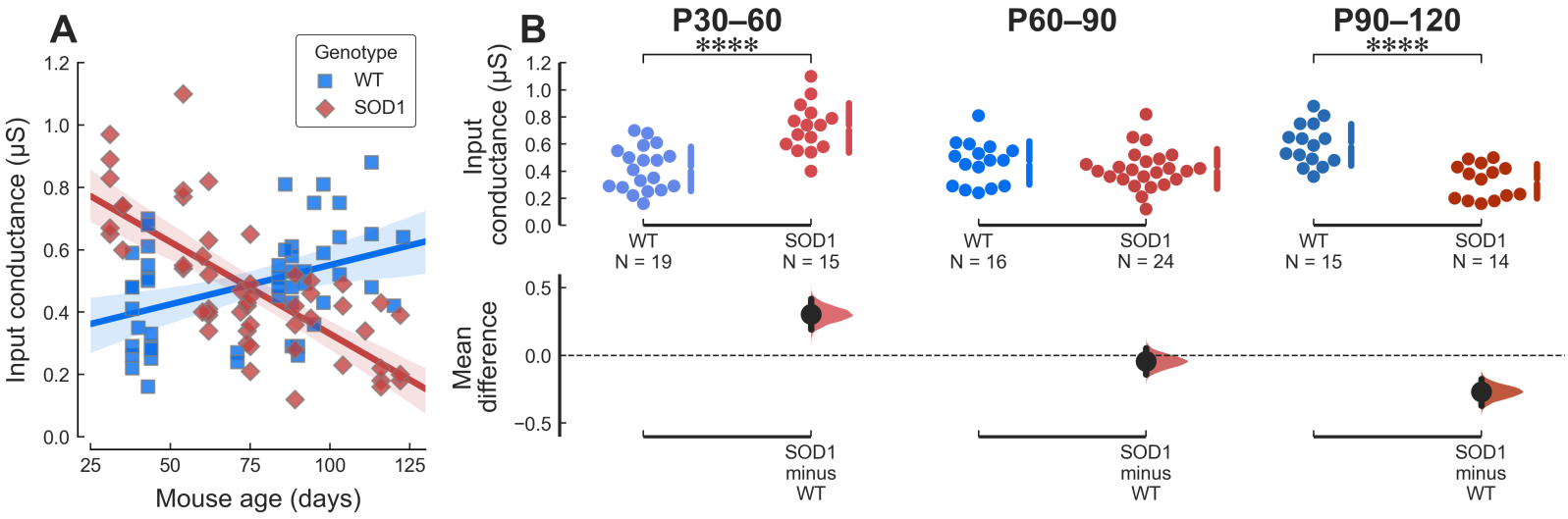
A
Genotype
WT
SOD1
Input conductance (µS)
Mouse age (days)
B
P30–60
P60–90
P90–120
****
****
Input conductance (µS)
WT
N = 19
SOD1
N = 15
WT
N = 16
SOD1
N = 24
WT
N = 15
SOD1
N = 14
Mean difference
SOD1 minus WT
SOD1 minus WT
SOD1 minus WT

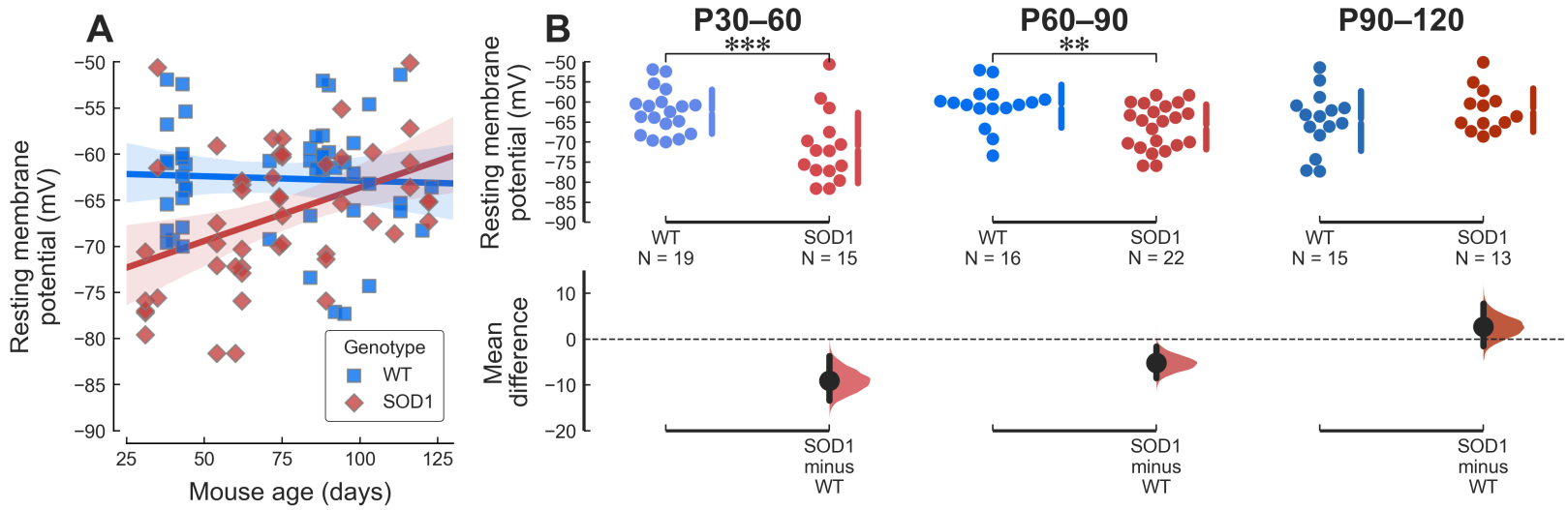
A
Resting membrane potential (mV)
−50
−55
−60
−65
−70
−75
−80
−85
−90
25
50
75
100
125
Mouse age (days)
Genotype
WT
SOD1
B
P30–60
P60–90
P90–120
***
**
Resting membrane potential (mV)
WT
N = 19
SOD1
N = 15
WT
N = 16
SOD1
N = 22
WT
N = 15
SOD1
N = 13
Mean difference
10
0
−10
−20
SOD1 minus WT
SOD1 minus WT
SOD1 minus WT

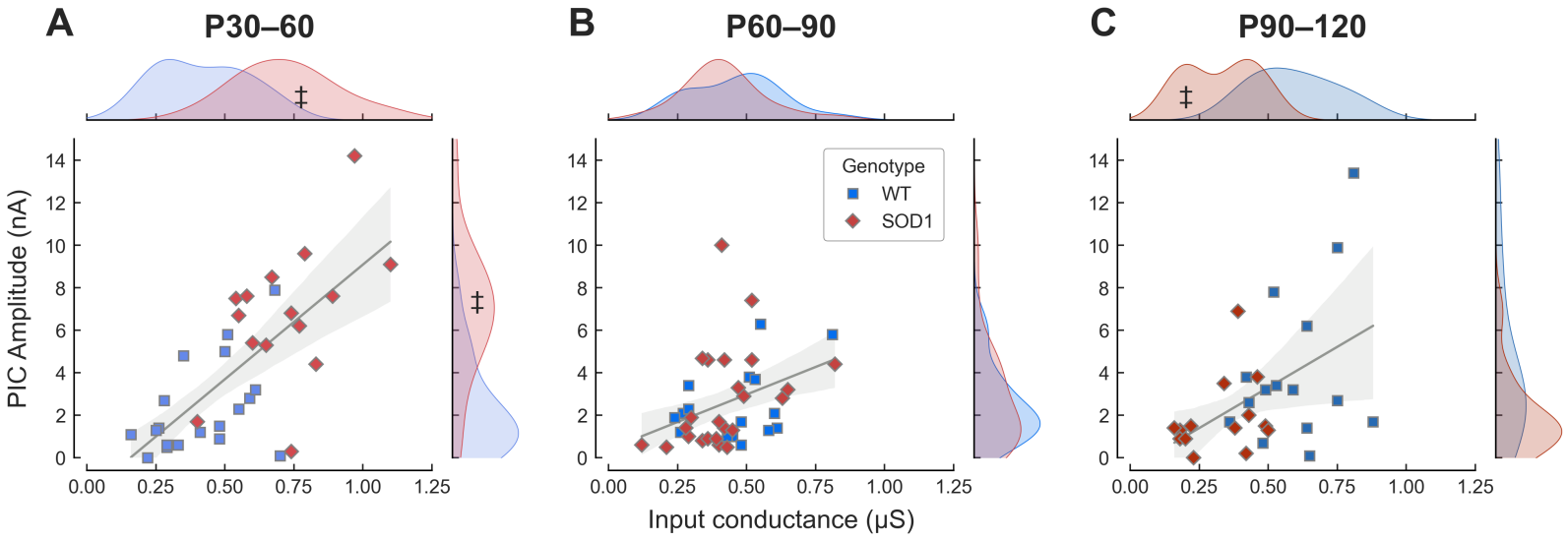
A
P30–60
B
P60–90
C
P90–120
‡
‡
‡
PIC Amplitude (nA)
Input conductance (μS)
Genotype
WT
SOD1
0
2
4
6
8
10
12
14
0.00
0.25
0.50
0.75
1.00
1.25

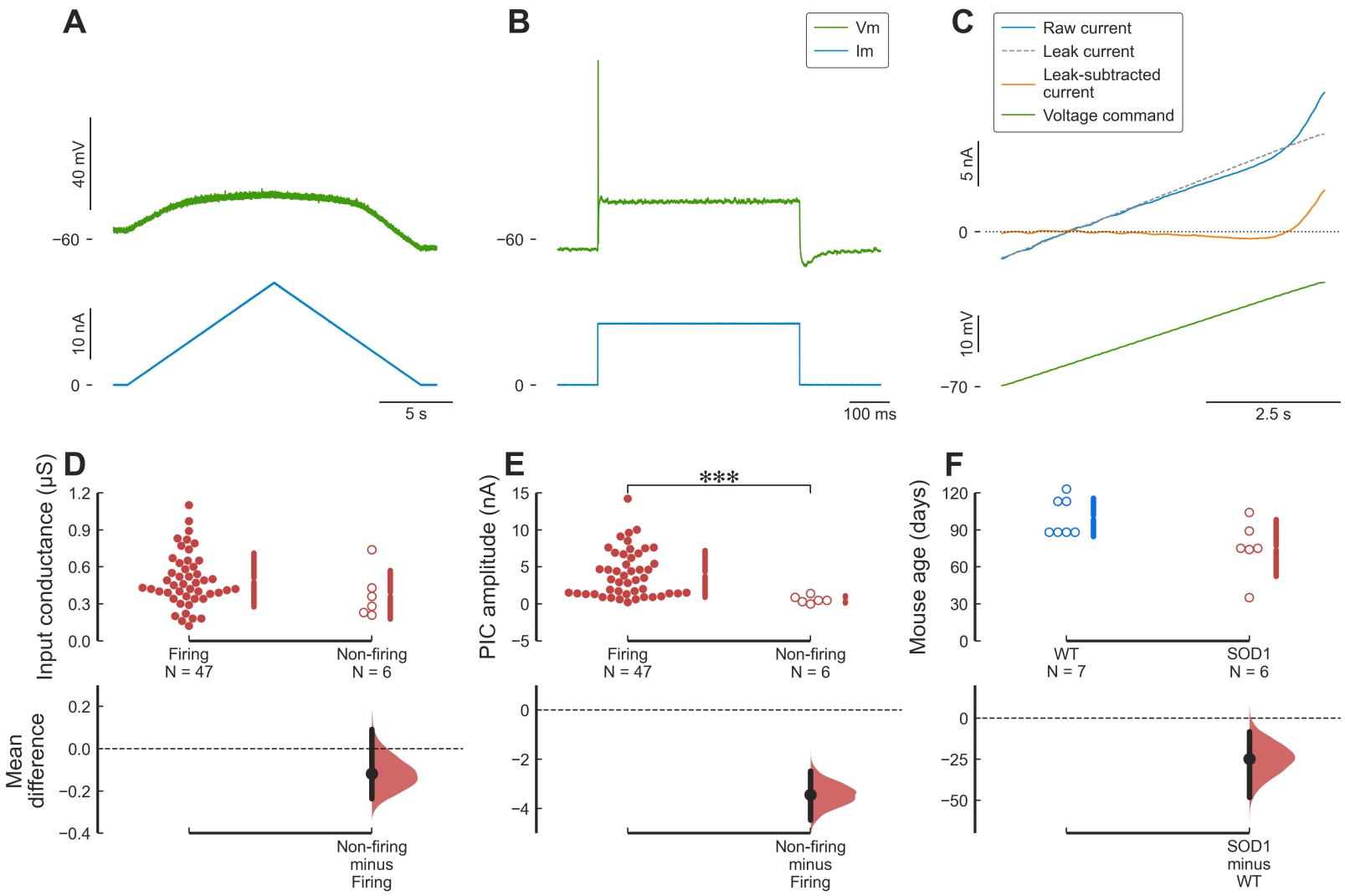
A
40 mV
−60
10 nA
0
5 s
B
Vm
Im
−60
0
100 ms
C
Raw current
Leak current
Leak-subtracted current
Voltage command
5 nA
0
10 mV
−70
2.5 s
D
Input conductance (µS)
1.2
0.9
0.6
0.3
0.0
Firing
N = 47
Non-firing
N = 6
Mean difference
0.2
0.0
−0.2
−0.4
Non-firing minus Firing
E
PIC amplitude (nA)
***
15
10
5
0
−5
Firing
N = 47
Non-firing
N = 6
0
−2
−4
Non-firing minus Firing
F
Mouse age (days)
120
90
60
30
0
WT
N = 7
SOD1
N = 6
0
−25
−50
SOD1 minus WT

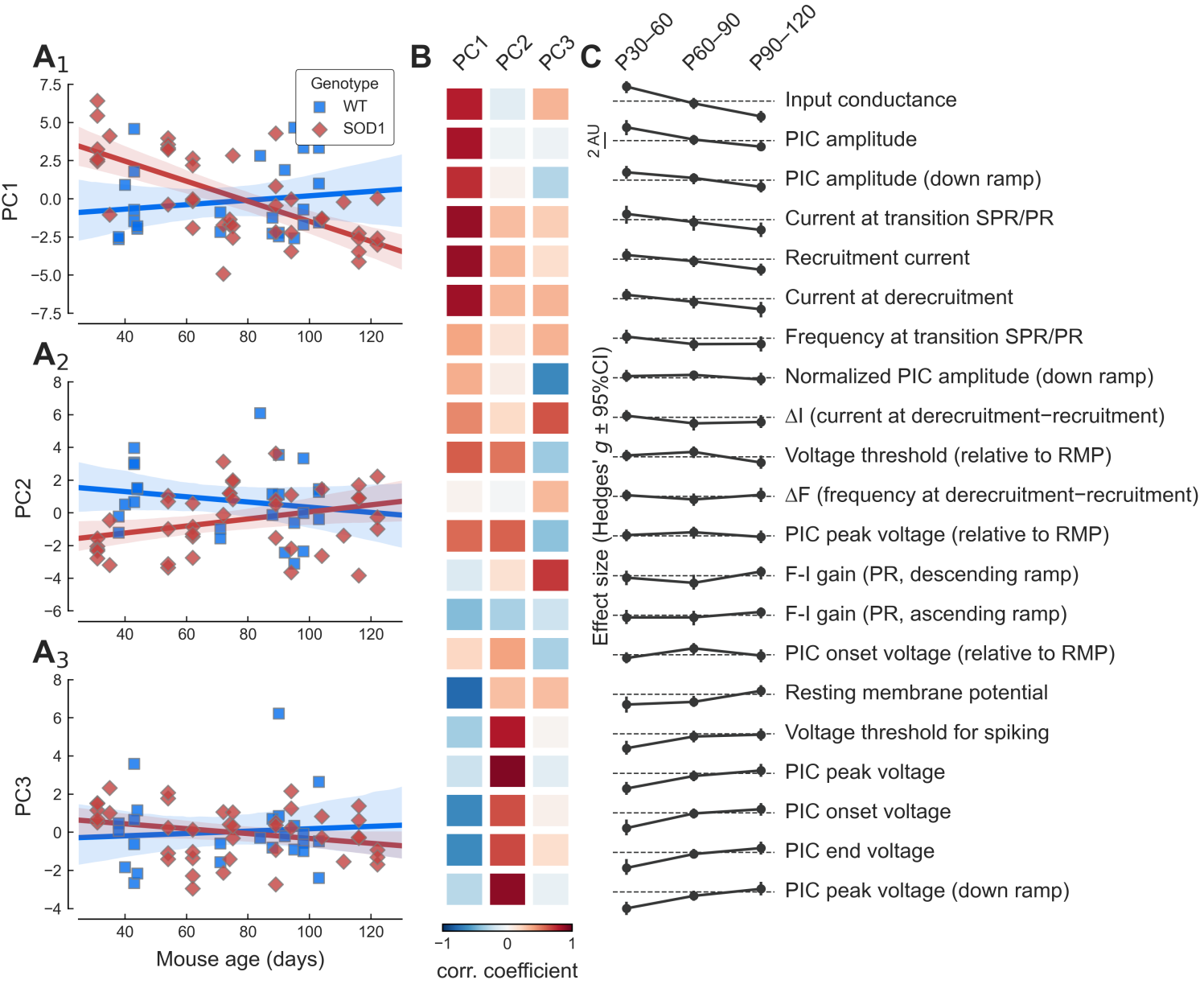
A1
A2
A3
Genotype
WT
SOD1
PC1
PC2
PC3
Mouse age (days)
B
PC1
PC2
PC3
corr. coefficient
C
P30–60
P60–90
P90–120
Effect size (Hedges' g ± 95%CI)
2 AU
Input conductance
PIC amplitude
PIC amplitude (down ramp)
Current at transition SPR/PR
Recruitment current
Current at derecruitment
Frequency at transition SPR/PR
Normalized PIC amplitude (down ramp)
ΔI (current at derecruitment−recruitment)
Voltage threshold (relative to RMP)
ΔF (frequency at derecruitment−recruitment)
PIC peak voltage (relative to RMP)
F-I gain (PR, descending ramp)
F-I gain (PR, ascending ramp)
PIC onset voltage (relative to RMP)
Resting membrane potential
Voltage threshold for spiking
PIC peak voltage
PIC onset voltage
PIC end voltage
PIC peak voltage (down ramp)

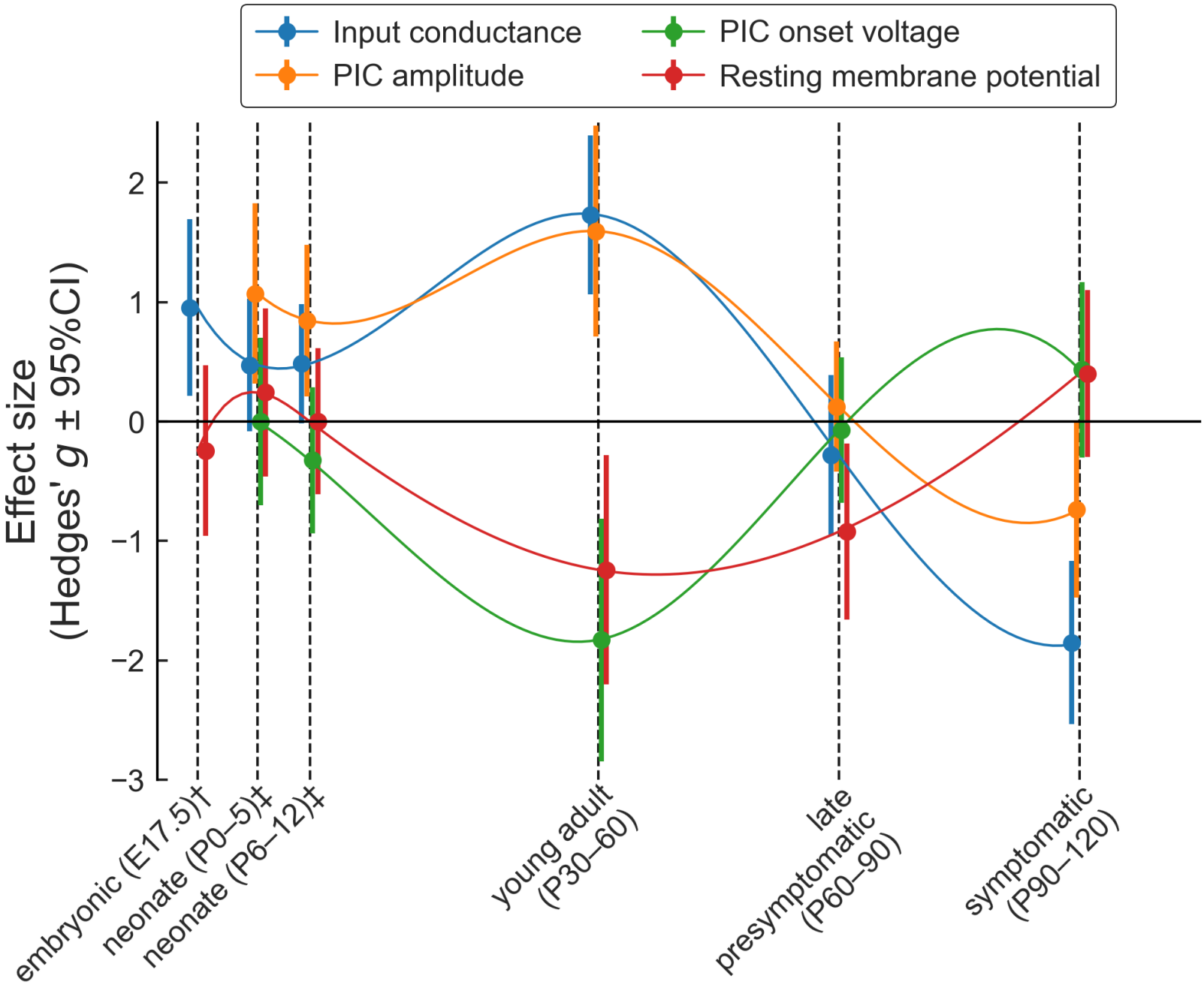
Input conductance
PIC amplitude
PIC onset voltage
Resting membrane potential
Effect size
(Hedges' g ± 95%CI)
2
1
0
−1
−2
−3
embryonic (E17.5)†
neonate (P0–5)‡
neonate (P6–12)‡
young adult
(P30–60)
late
presymptomatic
(P60–90)
symptomatic
(P90–120)

	P30–60				P60–90				P90–120			
	WT (N=19)	**SOD1 (N=15)**	**Mean diff.**	**Hedges' g**	**WT (N=16)**	**SOD1 (N=24)**	**Mean diff.**	**Hedges' g**	**WT (N=15)**	**SOD1 (N=14)**	**Mean diff.**	**Hedges' g**
Input conductance	0.42±0.16 µS [0.35–0.49]	0.72±0.18 µS [0.64–0.82]	0.30 µS [0.19–0.42] (p=2.2e−05 ****)	1.73 [0.93–2.40]	0.46±0.16 µS [0.39–0.54]	0.42±0.15 µS [0.36–0.48]	−0.04 µS [−0.14–0.05] (p=0.39)	−0.28 [−0.96–0.39]	0.60±0.15 µS [0.53–0.67]	0.33±0.13 µS [0.26–0.39]	−0.27 µS [−0.37–−0.17] (p=2.1e−05 ****)	−1.85 [−2.57–−1.17]
PIC amplitude	2.30±2.17 nA [1.52–3.45]	6.73±3.28 nA [5.18–8.51]	4.43 nA [2.56–6.29] (p=0.00016 ***)	1.59 [0.62–2.48]	2.47±1.69 nA [1.81–3.51]	2.75±2.40 nA [1.97–3.89]	0.27 nA [−0.93–1.53] (p=0.67)	0.12 [−0.53–0.67]	4.12±3.69 nA [2.67–6.40]	1.90±1.78 nA [1.24–3.19]	−2.22 nA [−4.63–−0.41] (p=0.05)	−0.74 [−1.27–0.00]
PIC amplitude (down ramp)	2.65±2.60 nA [1.76–4.16]	5.55±3.48 nA [4.01–7.45]	2.90 nA [0.86–4.89] (p=0.013 *)	0.94 [0.15–1.70]	2.29±2.30 nA [1.52–4.01]	2.87±2.22 nA [2.12–3.87]	0.58 nA [−1.03–1.76] (p=0.44)	0.25 [−0.50–0.82]	4.43±3.10 nA [3.03–6.09]	2.25±1.98 nA [1.48–3.56]	−2.18 nA [−3.99–−0.34] (p=0.032 *)	−0.81 [−1.49–−0.03]
Current at transition SPR/PR	5.93±3.24 nA [4.37–8.51]	8.01±2.67 nA [6.54–9.24]	2.08 nA [−0.95–4.08] (p=0.13)	0.69 [−0.48–1.68]	6.28±3.92 nA [4.32–9.67]	5.23±3.30 nA [3.99–7.23]	−1.04 nA [−4.72–1.39] (p=0.53)	−0.29 [−1.34–0.48]	5.90±2.70 nA [4.24–7.38]	2.70±2.34 nA [1.18–3.76]	−3.20 nA [−5.24–−1.28] (p=0.0081 **)	−1.23 [−2.07–−0.35]
Recruitment current	4.73±3.14 nA [3.50–6.23]	6.21±2.51 nA [4.77–7.27]	1.49 nA [−0.65–3.22] (p=0.14)	0.50 [−0.25–1.26]	5.28±2.64 nA [4.19–6.79]	4.53±3.38 nA [3.35–6.35]	−0.76 nA [−2.57–1.27] (p=0.46)	−0.24 [−0.94–0.43]	5.43±3.07 nA [4.07–7.16]	2.19±1.56 nA [1.59–3.32]	−3.24 nA [−4.98–−1.63] (p=0.0017 **)	−1.26 [−1.96–−0.52]
Current at derecruitment	5.92±3.76 nA [4.38–7.65]	7.64±3.31 nA [5.91–9.24]	1.72 nA [−0.73–3.94] (p=0.17)	0.47 [−0.24–1.19]	6.54±4.07 nA [4.69–9.12]	5.01±4.05 nA [3.54–7.04]	−1.53 nA [−4.41–1.18] (p=0.31)	−0.37 [−1.16–0.33]	5.64±2.95 nA [4.03–7.22]	2.59±1.58 nA [1.93–3.64]	−3.05 nA [−4.75–−1.24] (p=0.0056 **)	−1.26 [−2.23–−0.37]
Frequency at transition SPR/PR	54.30±17.35 Hz [45.49–66.17]	57.90±17.06 Hz [49.74–66.74]	3.60 Hz [−10.88–15.87] (p=0.62)	0.20 [−0.65–1.04]	53.55±13.32 Hz [44.57–62.21]	43.75±13.55 Hz [36.99–49.60]	−9.79 Hz [−20.63–0.31] (p=0.11)	−0.70 [−1.52–0.09]	51.58±15.41 Hz [41.70–59.94]	42.44±11.34 Hz [36.74–48.89]	−9.14 Hz [−19.10–1.70] (p=0.13)	−0.67 [−1.58–0.23]
Normalized PIC amplitude (down ramp)	6.72±5.77 nA/µS [4.50–9.57]	7.85±4.85 nA/µS [5.49–10.58]	1.13 nA/µS [−2.42–4.63] (p=0.56)	0.20 [−0.48–0.96]	5.05±4.43 nA/µS [3.38–7.73]	6.81±5.14 nA/µS [5.24–9.34]	1.75 nA/µS [−1.16–4.57] (p=0.26)	0.35 [−0.35–0.89]	7.77±5.24 nA/µS [5.46–10.56]	6.72±4.91 nA/µS [4.77–9.82]	−1.05 nA/µS [−4.38–2.82] (p=0.58)	−0.20 [−0.92–0.60]
ΔI (current at derecruitment−recruitment)	1.20±1.20 nA [0.69–1.74]	1.45±1.25 nA [0.89–2.17]	0.25 nA [−0.54–1.10] (p=0.57)	0.20 [−0.49–0.87]	1.47±1.83 nA [0.57–2.52]	0.42±1.10 nA [−0.01–0.94]	−1.04 nA [−2.22–−0.05] (p=0.093)	−0.72 [−1.57–0.05]	0.98±1.32 nA [0.38–1.78]	0.39±0.63 nA [0.05–0.71]	−0.58 nA [−1.50–0.13] (p=0.18)	−0.55 [−1.28–0.27]
Voltage threshold (relative to RMP)	17.03±6.37 mV [14.16–19.76]	18.09±5.21 mV [15.10–20.44]	1.05 mV [−3.07–4.74] (p=0.61)	0.17 [−0.53–0.86]	15.59±5.54 mV [13.26–18.55]	19.26±6.29 mV [16.80–22.24]	3.67 mV [−0.33–7.32] (p=0.072)	0.60 [−0.13–1.26]	17.10±5.54 mV [14.32–19.66]	13.79±3.62 mV [12.09–15.77]	−3.31 mV [−6.66–0.11] (p=0.071)	−0.67 [−1.44–0.15]
ΔF (frequency at derecruitment−recruitment)	1.79±13.96 Hz [−5.29–7.01]	3.77±11.06 Hz [−1.51–9.55]	1.98 Hz [−5.93–10.90] (p=0.65)	0.15 [−0.56–0.80]	6.53±17.29 Hz [0.25–21.46]	1.93±8.73 Hz [−1.51–6.16]	−4.60 Hz [−19.62–2.62] (p=0.4)	−0.36 [−1.12–0.37]	−0.85±7.97 Hz [−4.64–4.12]	0.75±7.97 Hz [−3.66–4.64]	1.60 Hz [−5.07–7.19] (p=0.62)	0.19 [−0.66–1.04]
PIC peak voltage (relative to RMP)	18.32±7.08 mV [15.26–21.42]	19.13±8.15 mV [14.28–22.51]	0.81 mV [−4.99–5.20] (p=0.76)	0.10 [−0.61–0.82]	18.09±7.71 mV [15.11–22.59]	21.18±5.82 mV [19.14–23.99]	3.09 mV [−1.76–6.94] (p=0.19)	0.45 [−0.34–1.10]	16.37±8.32 mV [12.41–20.31]	15.60±5.86 mV [12.55–18.63]	−0.77 mV [−6.08–4.36] (p=0.78)	−0.10 [−0.87–0.66]
F-I gain (PR, descending ramp)	19.21±10.07 Hz/nA [15.19–29.17]	17.23±5.15 Hz/nA [14.91–20.03]	−1.98 Hz/nA [−12.04–2.61] (p=0.58)	−0.25 [−1.15–0.58]	33.93±35.75 Hz/nA [18.24–75.19]	15.25±8.95 Hz/nA [11.99–21.30]	−18.68 Hz/nA [−59.63–−2.66] (p=0.22)	−0.88 [−1.69–0.11]	15.15±7.14 Hz/nA [11.73–20.87]	20.05±11.30 Hz/nA [15.50–28.05]	4.90 Hz/nA [−2.37–12.22] (p=0.23)	0.48 [−0.48–1.07]
F-I gain (PR, ascending ramp)	9.30±3.58 Hz/nA [7.08–11.31]	8.30±3.37 Hz/nA [6.42–9.86]	−1.00 Hz/nA [−3.68–1.83] (p=0.5)	−0.28 [−1.09–0.63]	12.18±7.30 Hz/nA [8.81–19.47]	10.28±6.43 Hz/nA [8.15–15.26]	−1.90 Hz/nA [−8.81–2.94] (p=0.54)	−0.27 [−1.23–0.53]	8.01±3.16 Hz/nA [6.33–10.08]	10.84±9.13 Hz/nA [7.69–19.20]	2.84 Hz/nA [−0.81–10.27] (p=0.31)	0.38 [−0.41–0.94]
PIC onset voltage (relative to RMP)	4.36±5.66 mV [1.69–6.68]	2.05±5.38 mV [−1.02–4.23]	−2.31 mV [−6.23–1.00] (p=0.23)	−0.41 [−1.05–0.28]	1.76±5.75 mV [−0.85–4.65]	6.12±5.54 mV [3.80–8.38]	4.36 mV [0.56–7.69] (p=0.025 *)	0.76 [0.01–1.40]	1.57±5.10 mV [−0.86–4.11]	0.92±5.94 mV [−1.76–4.48]	−0.64 mV [−4.57–3.45] (p=0.76)	−0.11 [−0.93–0.64]
Resting membrane potential	−62.38±5.52 mV [−64.71–−59.91]	−71.45±8.78 mV [−75.13–−66.37]	−9.07 mV [−13.37–−3.66] (p=0.002 **)	−1.24 [−2.19–−0.28]	−60.98±5.35 mV [−63.81–−58.71]	−66.18±5.63 mV [−68.56–−63.88]	−5.20 mV [−8.47–−1.59] (p=0.0067 **)	−0.92 [−1.54–−0.19]	−64.71±7.42 mV [−68.61–−61.39]	−61.99±5.43 mV [−64.41–−58.61]	2.72 mV [−1.57–7.73] (p=0.27)	0.40 [−0.32–1.10]

Voltage threshold for spiking	−45.35±5.48 mV [−47.79–−43.03]	−54.86±5.15 mV [−57.21–−52.17]	−9.51 mV [−12.79–−5.75] (p=1.9e−05 ****)	−1.74 [−2.53–−0.84]	−45.39±7.04 mV [−49.10–−42.26]	−47.53±5.85 mV [−49.76–−44.73]	−2.14 mV [−6.20–2.13] (p=0.34)	−0.33 [−1.04–0.38]	−47.61±5.00 mV [−49.94–−45.17]	−48.20±5.41 mV [−50.94–−45.31]	−0.59 mV [−4.24–2.98] (p=0.77)	−0.11 [−0.85–0.63]
PIC peak voltage	−43.83±4.79 mV [−45.74–−41.49]	−52.32±4.20 mV [−54.10–−50.00]	−8.49 mV [−11.41–−5.52] (p=4.8e−06 ****)	−1.83 [−2.60–−1.03]	−42.89±6.94 mV [−45.81–−39.26]	−44.88±5.24 mV [−46.93–−42.88]	−1.98 mV [−6.20–1.50] (p=0.34)	−0.33 [−0.97–0.33]	−48.34±5.89 mV [−50.89–−45.11]	−46.24±6.27 mV [−49.56–−43.26]	2.10 mV [−2.40–6.21] (p=0.36)	0.34 [−0.43–1.15]
PIC onset voltage	−58.03±6.35 mV [−60.91–−55.34]	−69.41±5.71 mV [−71.66–−66.01]	−11.38 mV [−14.95–−7.18] (p=5.1e−06 ****)	−1.83 [−2.69–−0.81]	−59.22±4.88 mV [−61.96–−57.18]	−59.66±6.39 mV [−61.98–−56.91]	−0.43 mV [−3.71–3.21] (p=0.81)	−0.07 [−0.70–0.54]	−63.15±6.31 mV [−65.99–−59.85]	−60.12±7.25 mV [−63.92–−56.48]	3.03 mV [−1.95–7.63] (p=0.24)	0.43 [−0.35–1.17]
PIC end voltage	−58.67±6.87 mV [−61.68–−55.65]	−71.37±6.36 mV [−73.99–−67.60]	−12.69 mV [−16.68–−8.02] (p=4.1e−06 ****)	−1.86 [−2.69–−0.80]	−60.48±4.90 mV [−63.57–−58.66]	−61.80±7.27 mV [−64.75–−58.95]	−1.32 mV [−4.61–2.66] (p=0.5)	−0.20 [−0.77–0.42]	−65.00±5.70 mV [−67.79–−62.19]	−61.30±8.12 mV [−65.34–−57.16]	3.70 mV [−1.44–8.54] (p=0.17)	0.52 [−0.28–1.27]
PIC peak voltage (down ramp)	−43.73±4.89 mV [−45.62–−41.28]	−53.63±4.90 mV [−55.76–−50.95]	−9.90 mV [−13.10–−6.60] (p=2.1e−06 ****)	−1.97 [−2.78–−1.17]	−42.49±8.15 mV [−45.71–−37.94]	−45.85±6.11 mV [−48.41–−43.56]	−3.36 mV [−8.41–0.62] (p=0.17)	−0.47 [−1.08–0.16]	−48.14±5.25 mV [−50.45–−45.05]	−45.98±6.26 mV [−49.54–−43.13]	2.17 mV [−2.22–5.96] (p=0.32)	0.37 [−0.41–1.20]